



# VNCCD: A gearbox fault diagnosis technique under nonstationary conditions via virtual decoupled transfer path

Cai Li, Penghong Lu, Gang Chen \*

Shien-Ming Wu School of Intelligent Engineering, South China University Of Technology, Guangzhou, 511442, China

## ARTICLE INFO

Communicated by J. JC

**Keywords:**

Gearbox fault diagnosis  
Non-stationary condition  
Transfer paths decoupling  
Nonlinear chirp mode component

## ABSTRACT

The interconnection between different components among a gearbox poses a challenge in decoupling vibration signals for fault diagnosis. This study presents a method called Virtual Non-Linear Chirp Component Decoupling (VNCCD) to address gearbox fault diagnosis. The method starts by identifying the decoupled frequency response function (DFRF) using a virtual decoupling method. The bearing force signals are then computed based on the DFRF, and the intrinsic signal components are extracted using a nonlinear chirp mode decomposition technique. The proposed approach enhances the quality of vibration signals in gear systems by eliminating the intercoupling effect of structural transfer paths. By employing the VNCCD method, the amplification of fault conditions can be effectively demonstrated compared to the nonlinear chirp component obtained from the original signal. Simulation and experimental results confirm the effectiveness of the VNCCD method in diagnosing gearbox systems that experience intricate structural transfer paths in nonstationary conditions.

## 1. Introduction

Parallel shaft gear systems are of significant importance across diverse industries including automotive, manufacturing, and Wind energy, owing to their exceptional transmission efficiency and extensive range of transmission ratios [1–4]. However, parallel shaft gearboxes frequently encounter challenging operating conditions, such as variable speed and overload, resulting in an inadequate operational lifespan that falls short of the intended longevity. As a consequence, substantial financial losses and serious accidents may ensue [5]. Therefore, fault diagnosis technology plays a crucial role in ensuring the operational reliability of gear systems.

Vibration signal measurements provide an effective means of assessing the operation of gear systems. In order to evaluate the performance of these systems, it is crucial to extract fault features from signals [6]. Classical signal processing methods, such as wavelet transform [7], Principal Component Analysis [8], time–frequency analysis [9] and sparse representation [10].

Due to the complex operational environment, the condition monitoring signals of gearbox systems exhibit nonstationary amplitude modulation and frequency modulation (AM-FM) characteristics, which are often referred to as nonlinear chirp signals. Practical nonlinear chirp signals (NCS) generally contain many nonstationary sub-signals (referred to as chirp modes), each of which usually contains valuable information related to the health condition of the machine [11,12]. Feature extraction and fault diagnosis methods for chirp components have been studied extensively in recent years. Chen [13] proposed the variational nonlinear chirp mode decomposition approach. This approach accurately estimates the instantaneous frequency (IF) of all components in nonstationary signals and extracts each component individually. Furthermore, Chen and colleagues also introduced the adaptive chirp mode decomposition [14,15] and intrinsic chirp component decomposition [16]. Additionally, order tracking techniques [17],

\* Corresponding author.

E-mail address: [gangchen@scut.edu.cn](mailto:gangchen@scut.edu.cn) (G. Chen).

empirical mode decomposition [18], and empirical wavelet transform [19] have been widely applied to fault diagnosis and condition monitoring of mechanical systems under nonstationary conditions. However, it is important to note that all of these techniques rely heavily on obtaining high-quality vibration signals. Analyzing poor-quality signals often leads to inaccurate judgments about the operation of gear systems.

In terms of the fault mechanism, gearbox vibrations primarily result from the contact between meshing gear teeth. Subsequently, these vibrations propagate through the housing, bearings, and shafts before being sensed by vibration sensors [20]. To capture vibration signals with distinct gear meshing features, sensors are typically positioned near the bearing block during tests. This placement ensures accurate detection of faults within the signals. Many researchers have focused on optimizing the placement of measurement points [21–24]. However, in highly complex and integrated mechanical systems, the number and locations of measuring points are often severely limited [25]. Moreover, during the transmission of vibrations, the intercoupling effects of structural transfer paths significantly alter or attenuate signal characteristics [26].

In order to mitigate the intercoupling effects of structural transfer paths, a better way is to construct the structural dynamic model of the whole structure by assembling the dynamic models of its simpler components (subsystems or substructures), transfer path analysis (TPA) serves as a valuable tool. Its primary application lies within the automotive engineering field, aiming to elucidate the generation and transmission of vibrations from both the excitation source and the transfer path [27,28]. Previous research has primarily modeled vibration transfer paths using frequency response functions or Markov parameter matrices [29]. Both methods require prior knowledge of the structure's vibration transfer paths. Quantitative studies on the impact of vibration transfer paths have been mostly in the field of automobile engineering, particularly for assessing each suspension's contribution to overall vibration levels [30,31]. Additionally, Vanhollebeke [27] et al. applied transfer path analysis to evaluate the effect of bearings on wind turbine gearbox vibrations. Research on gearbox transfer paths often focuses on vibration signal models, such as amplitude modulation described by the Hanning function [32]. However, these phenomenological models overlook specific structural characteristics, limiting their application in diagnosing complex gearbox faults. To address this difficulty, some researchers use bearing dynamic forces as the excitation sources and consider the mutual coupling effect among structural transfer paths [33,34].

The Frequency Response Functions (FRFs) act as a fundamental component of TPA for gear systems, establishing the physical connection between various parts [35]. The transfer function matrix can be obtained through two predominant methods: finite element Analysis and hammer impact testing. In previous work, Yu considered the mutual coupling effect of the transfer path model and introduced the notion of dynamic force in gearbox bearings [33,36]. By utilizing vibration signals, the dynamics of gearbox bearings can be identified, thus acquiring the FRFs matrix through FEA [37]. Nevertheless, as FEA is highly sensitive to boundary conditions and entails intricate modeling approaches, the hammer impact test serves as a commonly adopted alternative for obtaining the FRFs matrix in engineering applications.

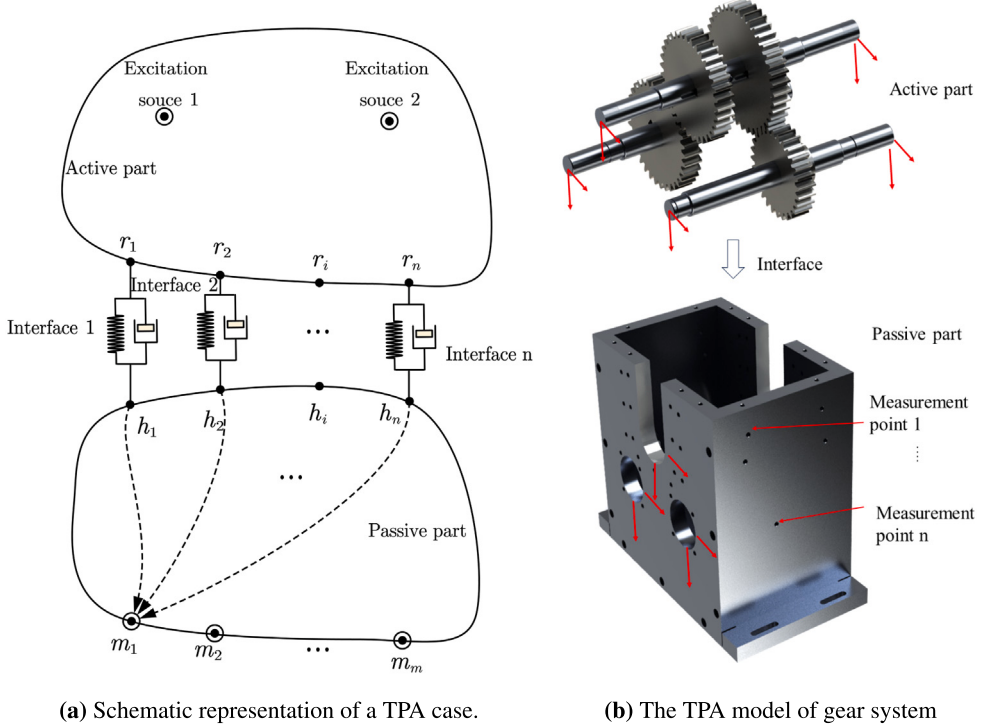
Due to the intricate structure of actual gear systems, obtaining the decoupled FRF of the gearbox housing is difficult (as it is typically measured after physically decoupling the gears and shafts). Besides the time-consuming testing process, physical decoupling can cause unforeseen changes in the assembly conditions. Recently, in-situ decoupling methods have been gaining increasing attention [38]. Based on the transfer path analysis theory, Laurent derived a theoretical model to obtain transfer functions without disassembling the substructure [39]. Wang proposed a generalized method utilizing in-situ transfer functions for predicting decoupled transfer functions [40]. Furthermore, Wang introduced an in-situ decoupling technique specifically designed for mechanical systems featuring rigid and resilient coupling links [41,42]. Huangfu employed the in-situ decoupling approach for fault tracking of gearboxes [34]. The aforementioned literature primarily utilizes the advantages of the virtual decoupling method: 1.it requires minimal system dynamic information and can handle internal degrees of freedom; 2.it offers superior applicability and versatility; 3.it does not require disassembling the structure, thereby ensuring high efficiency [43]. With the increasing integration and precision of industrial gear systems, these advantages hold significant potential value for engineering applications. However, to the best of our knowledge, the application of the virtual decoupling method for fault diagnosis of gearboxes under non-stationary conditions has not yet been investigated.

To address the aforementioned concerns, we propose a novel approach called Virtual Non-Linear Chirp Component Decoupling (VNCCD) for the extraction of decoupled non-linear chirp components from the bearing force response of a gear system. Firstly, the transfer path model of the gearbox is established, and based on this model, the virtual decoupling technique is introduced to acquire the Decoupled Frequency Response Functions (DFRFs) by mitigating the coupling effects of structural transfer paths without the need for physically disassembling the gear system. Subsequently, the identified bearing force signals in the frequency domain are obtained from the resulting frequency response functions, and the Inverse Fourier Transform (IFT) is employed to map these signals to the time domain. Finally, a signal decomposition method is utilized to extract the non-linear chirp components from these signals. Simulation and experimental results provide evidence that VNCCD is highly effective in diagnosing gear faults.

This paper is organized into six sections. Section 2 includes the theoretical fundamentals of gearbox transfer path analysis and virtual decoupling technology. Section 3 provides a detailed explanation of the gradual extraction process of non-linear chirp components through signal decomposition. In Section 4, a simulation example is presented to demonstrate the effectiveness of the proposed method. Section 5 showcases the validation of the proposed method through experimental studies. Lastly, Section 6 offers a summary of the conclusions drawn from this work.

## 2. Theoretical fundamental

TPA is a highly effective approach used to analyze vibration signals in gear systems [35]. In this method, the gear system and housing are simplified into a spring-damped model, which comprises active part, passive part, and measurement point. The resulting dynamic characteristics propagate through the transmission path of the passive part and impact the measurement point, as shown in Fig. 1.



(a) Schematic representation of a TPA case.

(b) The TPA model of gear system

**Fig. 1.** The TPA of the gearbox system. **Left:** The symbol  $r$  denotes the interface nodes located on the side of the rotor, while the  $h$  represents the interface nodes located on the side of the house. The symbol  $m_i$  represents the  $i$ th measurement point on the side of the house. **Right:** The top half of Fig. 1.b is the active part of the gear system, and the lower half of Fig. 1.b is passive part of the gear system.

## 2.1. Transfer path analysis of gear system

In this paper, our analysis focuses on a gearbox system, which is composed of an active part, a passive part, and a measurement point. The dynamic relationship among these three components is described by transfer path functions. Within this model, when a force  $\mathbf{F}$  is applied to the active part of the gearbox system, it induces vibrations resulting in a measured signal  $\mathbf{x}$  at the measurement point.

$$\mathbf{x} = \mathbf{H}\mathbf{f} \quad (1)$$

where  $\mathbf{F} = [f_1(\omega), f_2(\omega), \dots, f_m(\omega)]$  represents a set of  $m$  external generalized forces applied at various points within the active part, and  $\mathbf{x} = [x_1(\omega), x_2(\omega), \dots, x_n(\omega)]$  denotes  $n$  measured generalized displacements taken at different measurement points. The symbol  $\mathbf{H}$  represents the FRFs matrix between the active and passive parts.

According to transfer path analysis, the measured signal is composed of the contributions of the forces exerted by the active part through different bearings onto the passive part (gearbox house), transmitted to the measurement point via various transmission paths. Each individual contribution represents the effect of each bearing on the gearbox, and these contributions simultaneously act and couple with each other, forming the measured signal. Mathematically, this can be expressed as:

$$x_i = \sum_{j=1}^m H_{ij} f_j \quad (2)$$

where  $f_j$  stands for the  $j$ th generalized force acting on the active part,  $x_i$  is the  $i$ th generalized displacement of the measurement point,  $H_{ij}$  represents the FRFs between the  $j$ th action point on the active part and the  $i$ th measure point on the gearbox.

Research on bearing force signals began quite early and has achieved remarkable results [44]. However, earlier studies primarily focused on the bearings themselves. In recent years, in order to mitigate the intercoupling effects of structure transfer paths, this research has increasingly gained prominence in gearbox applications [36]. When the feature extraction task shifts from analyzing the vibration signal to examining the force signal exerted between the active and passive parts, the frequency response function matrix  $\mathbf{H}$  assumes a critically significant role [33]. However, the physical decoupling process is hampered by its inherent complexity, leading to time and resource inefficiencies. In order to achieve a straightforward and efficient decoupling method without compromising the integrity of the gearbox, we introduce the virtual decoupling approach in the subsequent subsection.

## 2.2. Frequency response function calculation by the virtual decoupling method

In order to establish a connection between the vibration signal and the bearing force signal, it is customary to acquire the FRFs between the designated measuring point and the passive component. Traditional physical decoupling has two major drawbacks: (1) it wastes time and resources, and (2) it reduces the system's lifespan and precision. [38]. In this section, we present the virtual decoupling approach as an alternative method to obtain the FRFs, obviating the need to dismantle the gear subsystem.

The connection of the active and passive components is abstracted linear spring-damp connection in this paper. The stiffness matrix of the spring is show as:

$$\mathbf{K}_b = \text{diag} ( k_1 \quad k_2 \quad \dots \quad k_j \quad \dots \quad k_n ) \quad (3)$$

where the stiffness of the  $i$ th spring is denoted by the symbol  $k_i$ . The number of transfer paths is indicated by the symbol  $n$ . On the rotor side, if the unitary force is applied to the interacting nodes, the deformation of the interfacing spring can be describable through the FRFs matrix:

$$\Delta \tilde{\mathbf{X}}(\omega) = (\mathbf{H}_{rr}^{\text{coup}}(\omega) - \mathbf{H}_{hr}^{\text{coup}}(\omega)) \mathbf{I}_{n \times n} = \begin{bmatrix} H_{r1r1}^{\text{coup}} - H_{h1r1}^{\text{coup}} & H_{r1r2}^{\text{coup}} - H_{h1r2}^{\text{coup}} & \dots & H_{r1rn}^{\text{coup}} - H_{h1rn}^{\text{coup}} \\ H_{r2r1}^{\text{coup}} - H_{h2r1}^{\text{coup}} & H_{r2r2}^{\text{coup}} - H_{h2r2}^{\text{coup}} & \dots & H_{r2rn}^{\text{coup}} - H_{h2rn}^{\text{coup}} \\ \dots & \dots & \dots & \dots \\ H_{rnr1}^{\text{coup}} - H_{hn1r1}^{\text{coup}} & H_{rnr2}^{\text{coup}} - H_{hn1r2}^{\text{coup}} & \dots & H_{rnnr}^{\text{coup}} - H_{hn1rn}^{\text{coup}} \end{bmatrix} \quad (4)$$

In the above instance, the side of the rotor is the point of force application, which is represented though the symbol  $\tilde{\mathbf{X}}$ . The unitary matrix with dimension of  $n \times n$  is denoted by  $\mathbf{I}$ . When the point of force action is at the  $i$ th point on the rotor,  $H_{rihj}^{\text{coup}}$  is the FRF of the force to the  $j$ th point on the house. When the force action point is at the  $i$ th point on the rotor,  $H_{rjri}^{\text{coup}}$  is the FRF at the  $j$ th point on the rotor. The coupled system is indicated by the superscript coup.  $\omega$  is omitted for writing convenience, but note that all of our analysis is in the frequency domain in this section.

Let  $\mathbf{F}_h$  represent the generalized force between the active part acting and the passive part. The responses of measurement points can be expressed as:

$$\tilde{\mathbf{X}}_m = \mathbf{H}_{mh}^{\text{Decoup}} \mathbf{F}_h = \mathbf{H}_{mh}^{\text{Decoup}} \mathbf{K}_b \Delta \tilde{\mathbf{X}} \quad (5)$$

In this context, the subscript  $m$  indicates the measurement point, while the superscript "Decoup" denotes the decoupled system:

$$\tilde{\mathbf{X}}_m = \mathbf{H}_{mr}^{\text{coup}} \mathbf{I}_{n \times b} \quad (6)$$

Bring the formula (4), (5), (6) in it, we have:

$$\mathbf{H}_{mr}^{\text{coup}} = \mathbf{H}_{mh}^{\text{Decoup}} \mathbf{K}_b (\mathbf{H}_{rr}^{\text{coup}} - \mathbf{H}_{hr}^{\text{coup}}) \quad (7)$$

The following is an expression of the FRF matrix at the house side between the measurement points and the nodes:

$$\mathbf{G}_{mh} = \mathbf{H}_{mh}^{\text{Decoup}} \mathbf{K}_b = \mathbf{H}_{mh}^{\text{coup}} (\mathbf{H}_{rr}^{\text{coup}} - \mathbf{H}_{hr}^{\text{coup}})^{-1} \quad (8)$$

When the unitary force  $\mathbf{I}$  acts upon the interfacing node on the housing side, the resulting displacement change in the interfacial spring can be represented as follows

$$\Delta \hat{\mathbf{X}} = (\mathbf{H}_{rh}^{\text{coup}} - \mathbf{H}_{hh}^{\text{coup}}) \mathbf{I}_{n \times n} = \begin{bmatrix} H_{r1h1}^{\text{coup}} - H_{h1h1}^{\text{coup}} & H_{r1h2}^{\text{coup}} - H_{h1h2}^{\text{coup}} & \dots & H_{r1hn}^{\text{coup}} - H_{h1hn}^{\text{coup}} \\ H_{r2h1}^{\text{coup}} - H_{h2h1}^{\text{coup}} & H_{r2h2}^{\text{coup}} - H_{h2h2}^{\text{coup}} & \dots & H_{r2hn}^{\text{coup}} - H_{h2hn}^{\text{coup}} \\ \dots & \dots & \dots & \dots \\ H_{rnh1}^{\text{coup}} - H_{hn1h1}^{\text{coup}} & H_{rnh2}^{\text{coup}} - H_{hn1h2}^{\text{coup}} & \dots & H_{rnnh}^{\text{coup}} - H_{hn1hn}^{\text{coup}} \end{bmatrix} \quad (9)$$

The displacement change of the target point can be expressed [40]:

$$\hat{\mathbf{X}}_m = \mathbf{H}_{mh}^{\text{Decoup}} \mathbf{K}_b \Delta \hat{\mathbf{X}} + \mathbf{H}_{mh}^{\text{Decoup}} \mathbf{I}_{n \times n} \quad (10)$$

The coupled frequency response function linking the measurement points to the interfacing nodes on the housing side can be derived:

$$\mathbf{H}_{mh}^{\text{coup}} = \mathbf{H}_{mh}^{\text{Decoup}} \mathbf{K}_b (\mathbf{H}_{rh}^{\text{coup}} - \mathbf{H}_{hh}^{\text{coup}}) + \mathbf{H}_{mh}^{\text{coup}} \quad (11)$$

Combining Eqs. (9), (10), and (11), the decoupled FRF from the points of measurement to the housing side interface nodes can easily be expressed as follows:

$$\mathbf{H}_{mh}^{\text{Decoup}} = \mathbf{H}_{mh}^{\text{coup}} - \mathbf{H}_{mr}^{\text{coup}} (\mathbf{H}_{rr}^{\text{coup}} - \mathbf{H}_{hr}^{\text{coup}})^{-1} (\mathbf{H}_{rh}^{\text{coup}} - \mathbf{H}_{hh}^{\text{coup}}) \quad (12)$$

### 2.3. The solution of inverse problem of dynamic

Initially, obtaining the bearing force in the frequency domain is equivalent to solving the dynamic inverse problem using the corresponding Eq. (1). Notably, the condition number of the FRFs matrix is usually very large, and it is often a non-square matrix. To address the dynamic inverse problem, an adjustment is applied to Eq. (1), yielding:

$$(\mathbf{H}_{\text{mh}}^{\text{Decoup}})^T \mathbf{x} = (\mathbf{H}_{\text{mh}}^{\text{Decoup}})^T (\mathbf{H}_{\text{mh}}^{\text{Decoup}}) \mathbf{F} \quad (13)$$

Where the symbol "T" denotes the Hermitian transpose of the matrix. The superscript "Decoup" signifies the decoupled system. For the sake of simplicity, the superscript "Decoup" and subscript mh are omitted in this subsection.

Mathematically, the identification of bearing forces is equivalent to calculating the inversion of  $\mathbf{H}$ , which is ill-conditioned in engineering. Classic approaches to solving inverse dynamics problems are the Truncated Singular Value Decomposition (TSVD) [45] and Tikhonov regularization [46]. The former involves finding the optimal approximate solution algorithms after low-rank approximation of  $\mathbf{H}$ , while the latter introduces regularization terms, both resulting in biased estimates. Here, we introduce the Maximumly Weighted Iteration (MWI) method to address this issue. We provide pseudocode and proofs in the appendix. This method reduces the ill-conditioning of  $\mathbf{H}$  by introducing weighted matrices  $\mathbf{W}$  and theoretically proves that it yields unbiased estimates [47]. The weighted decomposition of  $\mathbf{F} = \mathbf{W}\mathbf{f}$  is considered, allowing for the formulation of Eq. (13), which can be described as follows:

$$\mathbf{H}^T \mathbf{x} = \mathbf{H}^T \mathbf{H} \mathbf{W} \mathbf{f} \quad (14)$$

For original formula(13), We obtain the following mathematical expression by considering the upper bound of error for:

$$\frac{\delta \mathbf{F}}{\mathbf{F}} \leq k(\tilde{\mathbf{A}}) \frac{\|\mathbf{A}\| \|\delta \mathbf{y}\|}{\|\mathbf{A}\| \|\mathbf{y}\|} + k(\tilde{\mathbf{A}}) \frac{\|\delta \mathbf{A}\|}{\|\tilde{\mathbf{A}}\|} \quad (15)$$

where  $k(\tilde{\mathbf{A}}) = \|\tilde{\mathbf{A}}\| \|\tilde{\mathbf{A}}^*\|$ ,  $\mathbf{A} = \mathbf{H}^T \mathbf{H}$  and  $\mathbf{y} = \mathbf{H}^T \mathbf{x}$ . The symbol  $\delta$  and  $\|\cdot\|$  stands for error and Frobenius norm of matrix.

When the symbol  $\mathbf{W}$  is employed to decrease the degree of ill-conditioning of  $\mathbf{H}^T \mathbf{H}$ , the upper bound of error can be derived:

$$\frac{\delta \mathbf{F}}{\mathbf{F}} \leq k(\tilde{\mathbf{A}} \mathbf{W}) \frac{\|\mathbf{A} \mathbf{W}\| \|\delta \mathbf{y}\|}{\|\mathbf{A} \mathbf{W}\| \|\mathbf{y}\|} + k(\tilde{\mathbf{A}} \mathbf{W}) \frac{\|\delta \mathbf{A} \mathbf{W}\|}{\|\tilde{\mathbf{A}} \mathbf{W}\|} \quad (16)$$

The following requirements need to be fulfilled in order to ensure that, after weighted decomposition, the upper bound of the identification error is decreased:

$$k(\tilde{\mathbf{A}} \mathbf{W}) \frac{\|\mathbf{A}\| \|\mathbf{W}\|}{\|\tilde{\mathbf{A}} \mathbf{W}\|} \leq k(\tilde{\mathbf{A}}) \frac{\|\mathbf{A}\|}{\|\tilde{\mathbf{A}}\|}, \quad k(\tilde{\mathbf{A}} \mathbf{W}) \frac{\|\delta \mathbf{A} \mathbf{W}\|}{\|\tilde{\mathbf{A}} \mathbf{W}\|} \leq k(\tilde{\mathbf{A}}) \frac{\|\mathbf{A}\|}{\|\tilde{\mathbf{A}}\|} \quad (17)$$

In this paper, the matrix  $\mathbf{W}$  is a diagonal matrix, where  $m$  is the dimension of square matrix. The matrix  $\mathbf{A} = \mathbf{H}^T \mathbf{H}$  is selected as:

$$\mathbf{W} = \text{diag}(w_1, w_2, \dots, w_m), w_k = \sqrt{\frac{\sum_{i=1}^m a_{ik}^2}{\sum_{i=1, j=1}^{m, m} a_{ij}^2}}, i = 1, 2, \dots, m \quad (18)$$

In the above equation,  $a_{ij}$  represents the element of matrix  $\mathbf{A}$ . The number  $\alpha$  is added for regularization to Eq. (14)

$$(\mathbf{H}^T \mathbf{H} \mathbf{W} + \alpha \mathbf{E}) \mathbf{f} = \mathbf{H}^T \mathbf{x} + \alpha \mathbf{f} \quad (19)$$

where the weighted factor  $\alpha$  is a regularization parameter and can be selected based on generalized cross validation (GCV)  $\alpha(\alpha > 0)$  [48]. Due to the matrix  $\mathbf{H}^T \mathbf{H} \mathbf{W}$  is semi-positive definite matrix, the condition number will decrease for  $\alpha$  [49]. The equation essentially serves as the coefficient matrix in the iterative solution of Eq. (19):

$$(\mathbf{H}^T \mathbf{H} \mathbf{W} + \alpha \mathbf{E}) \mathbf{f}^{(k+1)} = \mathbf{H}^T \mathbf{x} + \alpha \mathbf{f}^{(k)} \quad (20)$$

Assuming that after  $k$  iterations, the bearing dynamic forces  $\mathbf{F}$  have been reconstructed by:

$$\mathbf{F} = \mathbf{W} \mathbf{f}^{(k)} \quad (21)$$

At the present moment,  $\mathbf{F}$  represents a signal in the frequency domain. It is mapped to the time domain using the IFT:

$$[f_1, \dots, f_m]^T = [\frac{1}{2\pi} \int_{-\infty}^{\infty} f_1(\omega) e^{j\omega t} \dots \frac{1}{2\pi} \int_{-\infty}^{\infty} f_m(\omega) e^{j\omega t}]^T = \text{IFT}(\mathbf{F}) \quad (22)$$

### 3. Force signal non-linear chirp component extraction and fault diagnosis work flow

In practical systems, the fault signal typically comprises three primary constituents: the impulse component, the harmonic component, and the noise [50]. The harmonic component, known as the chirp component under nonstationary condition, exhibit frequency modulation and amplitude modulation that varies over time [51]. This component is associated with the operational frequency of the gear system and is often induced by mechanical system vibrations or rotations, such as gear failures [52].

Under non-stationary conditions, a complex signal is typically composed of multiple components, which often exhibit non-stationary and nonlinear characteristics. [6]. This means that each constituent part of the signal exhibits changes over time in terms of its amplitude and frequency. Each of these components can be thought of as an oscillatory mode with both amplitude

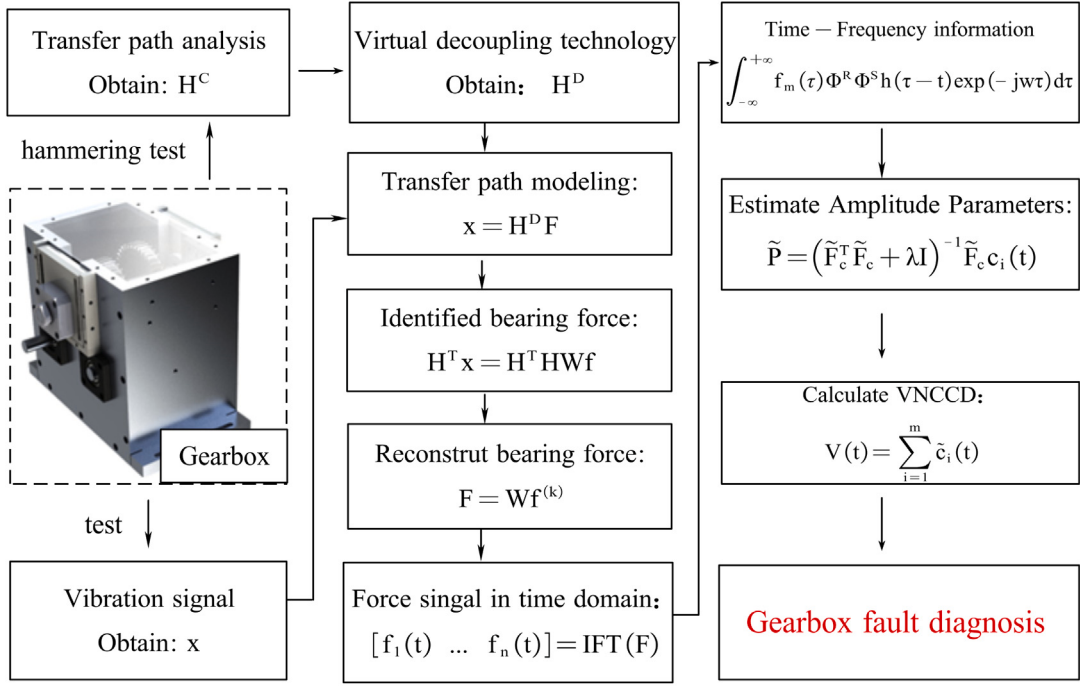


Fig. 2. The flow diagram of the proposed method.

modulation (AM) and frequency modulation (FM)(also known as chirp). Therefore, a multi-component signal can be represented as combination of various AM–FM components:

$$f = \sum_{i=1}^Q c_i(t) + n_i(t) = \sum_{i=1}^Q a_i(t) \cos(\omega_c(t) + \phi_i(t)dt) + n_i(t) \quad (23)$$

Where  $a_i(t)$  represents the instantaneous amplitude,  $\phi_i(t)$  denotes the instantaneous phase,  $\omega_c(t)$  stands for carrier frequency.  $Q$  indicates the number of the signal components.  $c_i$  represents the  $i$ th nonlinear chirp component of signal. According to the trigonometric equation, the Eq. (23) can be represented as:

$$c_i(t) = a_i(t) \cos(\omega_c(t) + \int_0^t \phi_i(t)dt) = u_{ci} \cos(\int_0^t \phi_i(t)dt) + v_{ci} \sin(\int_0^t \phi_i(t)dt) \quad (24)$$

Where  $u_{ci}(t) = a_i(t) \cos(\omega_c(t))$  and  $v_{ci}(t) = -a_i(t) \sin(\omega_c(t))$ . Taking into account the discretization of signal at specific sampling time  $t \in \{t_1, t_2, \dots, t_N\}$ , the amplitude functions  $u_{ci}(t)$ ,  $v_{ci}(t)$  and the IF  $\phi_i(t)$  is depicted as:

$$\begin{aligned} u_{ci} &= \mathbf{B}_c(t) \mathbf{P}_u \\ v_{ci} &= \mathbf{B}_c(t) \mathbf{P}_v \\ \phi_{ci} &= \mathbf{B}_\phi(t) \mathbf{P}_\phi \end{aligned} \quad (25)$$

Where  $\mathbf{B}_c(t) = [1, \cos(2\pi/T_0 t), \sin(2\pi/T_0 t), \dots, 1, \cos(2\pi/T_0 t), \sin(2\pi/T_0 t), \dots]$ ,  $l = 1, 2 \dots L_1$  and  $\mathbf{B}_\phi(t) = [1, \cos(2\pi/T_0 t), \sin(2\pi/T_0 t), \dots, 1, \cos(2\pi/T_0 t), \sin(2\pi/T_0 t), \dots]$ ,  $l = 1, 2 \dots L_2$  stands for the Redundant Fourier Basis functions.  $\mathbf{P}_u$ ,  $\mathbf{P}_v$  and  $\mathbf{P}_\phi$  stands for the corresponding parameter column vectors. The frequency resolution is  $T_0 = f_s/2N$ , and the sampling frequency is  $f_s$ . The parameters  $L_1$  and  $L_2$  indicate the orders of this model. Derived from formula (24), the signal model is represented in the following matrix form:

$$c_i(t) = \mathbf{F}_c \mathbf{P}_c \quad (26)$$

Where  $\mathbf{F}_c = \begin{bmatrix} \cos(2\pi \int_0^t \mathbf{B}_\phi(\tau) \mathbf{P}(\tau) d\tau) & \sin(2\pi \int_0^t \mathbf{B}_\phi(\tau) \mathbf{P}(\tau) d\tau) \end{bmatrix} \begin{bmatrix} \mathbf{B}_c & 0 \\ 0 & \mathbf{B}_c \end{bmatrix}$  and  $\mathbf{P}_c = \begin{bmatrix} \mathbf{P}_u \\ \mathbf{P}_v \end{bmatrix}$

The time-frequency distribution of  $f_m(t)$  is used for calculating the instantaneous frequency  $\phi(t)$ . General Parameterized Time-Frequency Transform(GPTF) [53] is utilized to yield a highly focused time-frequency distribution for  $\phi(t)$ :

$$\text{GPTF}(t, \omega) = \int_{-\infty}^{\infty} f_m(\tau) \Phi^R \Phi^S h(\tau - t) \exp(-j\omega\tau) d\tau \quad (27)$$

Where  $\Phi^R$  and  $\Phi^S$  represent the rotation and shift operators, respectively, based on the redundant Fourier kernel in GPTF transform,  $h(\tau - t)$  denotes window function. The matrix  $\mathbf{F}_c$  is determined using the estimated  $\phi(t)$ . Then the amplitude parameter  $\mathbf{P}_c$  is derived

by addressing the optimization model:

$$\tilde{\mathbf{P}}_c = \arg \min \|c_i(t) - \tilde{\mathbf{F}}_c \mathbf{P}_c\|_2^2 \quad (28)$$

The analytical solution of Eq. (28) can be derived:

$$\tilde{\mathbf{P}}_c = (\tilde{\mathbf{F}}_c^T \tilde{\mathbf{F}}_c + \lambda \mathbf{I})^{-1} \tilde{\mathbf{F}}_c^T c_i(t) \quad (29)$$

In this equation,  $\mathbf{I}$  is a unit matrix, the regularization parameter  $\lambda$  is selected via GCV. The  $m$ th nonlinear chirp component is reconstructed:

$$\tilde{c}_i(t) = \tilde{\mathbf{F}}_c \tilde{\mathbf{P}}_c \quad (30)$$

The VNCCDs are finally calculated as:

$$\mathbf{V}(t) = \sum_{i=1}^m \tilde{c}_i(t) \quad (31)$$

The Fig. 2 illustrates the calculation process flow diagram for the proposed method. The following is a summary of the method:

- (i) Step 1. (Raw data acquisition) In this step, the vibration response  $\mathbf{x}$  of the gearbox under nonstationary condition at measuring point is measured. Additionally, the coupled frequency response function  $\mathbf{H}^{\text{coup}}$  is estimated through hammer experiments. This step involves collecting the initial data needed for further analysis.
- (ii) Step 2. (DFRF calculation through virtual decoupling technology) Virtual decoupling technology is used to obtain the decoupled FRFs  $\mathbf{H}^{\text{Decoup}}$ .
- (iii) Step 3. (Bearing force estimation) The force signal  $\mathbf{F}$  is calculated using MWI and GCV approaches. This identification is based on the decoupled frequency response function  $\mathbf{H}^{\text{Decoup}}$  and the measured responses  $\mathbf{x}$ , allowing for the estimation of the forces affecting the gearbox.
- (iv) Step 4. (Bearing force in time domain) The IFT is used to map the reconstructed forces signals to the time domain.
- (v) Step 5. (Non-linear chirp component extraction): This step involves using GPTF to calculate the time-frequency distribution of the bearing force. Subsequently fitting the instantaneous frequency  $\tilde{c}_i(t)$  from  $\mathbf{GPTF}(t, \omega)$  and calculating  $\mathbf{V}(t)$ . Solve the optimization model for estimating the parameter  $\mathbf{P}_c$ , and extracting the  $m$ th intrinsic chirp component by  $\tilde{c}_i(t) = \tilde{\mathbf{F}}_c \tilde{\mathbf{P}}_c$ .
- (vi) Step 6. (Fault diagnosis) VNCCD may be computed by superimposing all  $m$  fault-related nonlinear chirp components. The gearbox can be diagnosed using the VNCCD.

#### 4. Simulation verification

In this section, we present a numerical illustration of the calculation process for the proposed method using a two-stage gear model. The dynamic model used in our study, as shown in Fig. 3, is a lumped parameter model representing a spur two-stage gear system. The pertinent differential equation and various parameters for this dynamic model are provided in the Appendix. To calculate the time-varying stiffness of a gear pair, we employ the potential energy method [54]. Additionally, the time-varying meshing damping can be computed using the method [55].

When a gear tooth with a crack engages in meshing within a gearbox, the time-varying meshing stiffness is reduced compared to the healthy condition. Consequently, as shown in Fig. 4(a), the outcomes consider the presence of a gear crack fault. The procedure for accelerating the driving shaft is depicted in Fig. 4(b). To solve the aforementioned time-dependent problem, we employ the Newmark approach.

##### 4.1. The numerical simulation and result of the virtual decoupling technology

In this instance, physical decoupling is defined as obtaining the decoupled FRFs directly from the dynamic matrix of passive part via Eq. (A.8). As though the active part has been removed from the system, the matrix of passive part contains known information. On the contrary, virtual decoupling technique involves using the system FRFs matrix Eq. (12) of (the coupled system) to calculate the decoupled FRF. As shown in Fig. 5, the FRFs obtained through the virtual decoupling approach is then compared with the FRFs obtained by the physical decoupling method. The measured FRF significantly approaches the theoretical one, as demonstrated by the results, indicating that the adopted virtual decoupling technique is acceptable.

##### 4.2. Extracting force non-linear chirp components for fault diagnosis

In order to illustrate the effects of our proposed approach, we first utilize the vibration signal at the measurement point for gearbox fault diagnosis. The theoretical vibration signal with the gear cracking fault condition and the healthy condition are displayed in Fig. 6(a). It is difficult to evaluate the working state of gear in the time domain. As shown in Fig. 6(b), order tracking, a mainstream technique for identifying faults under non-stationary conditions, faces difficulty in evaluating the gear operating condition. Therefore, it is extremely difficult to diagnose gear faults based on vibration signals alone.

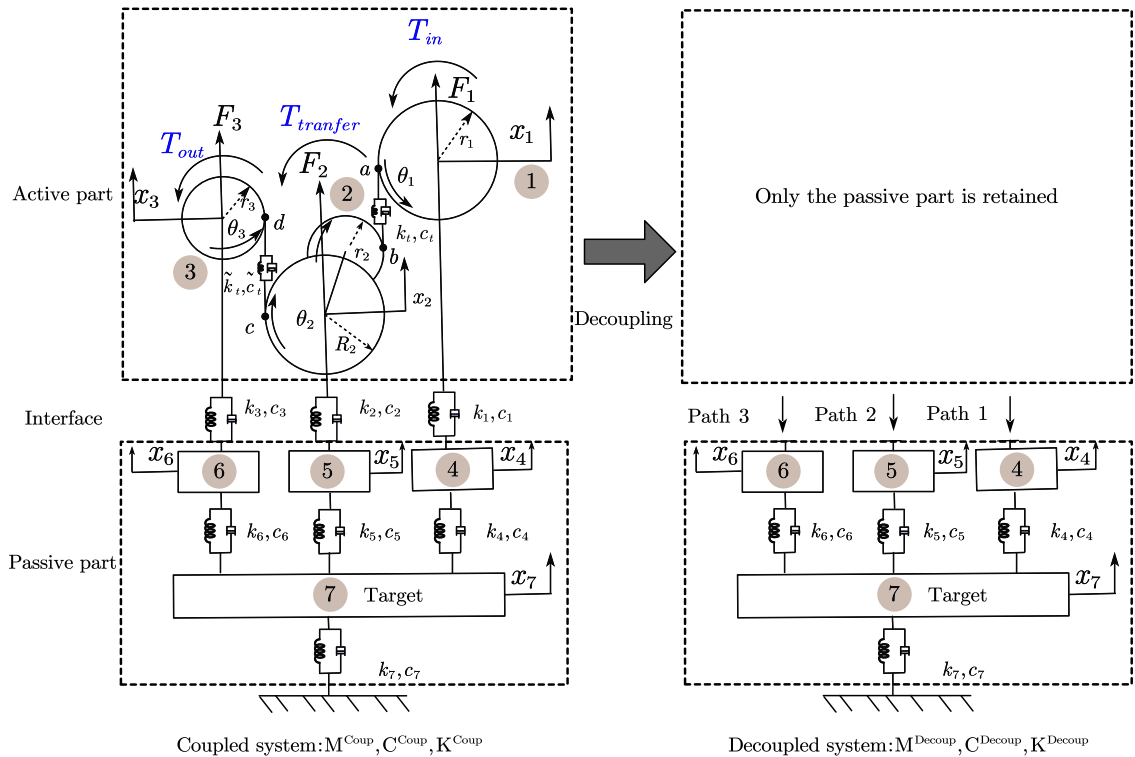


Fig. 3. The lumped parameter model in numerical example.

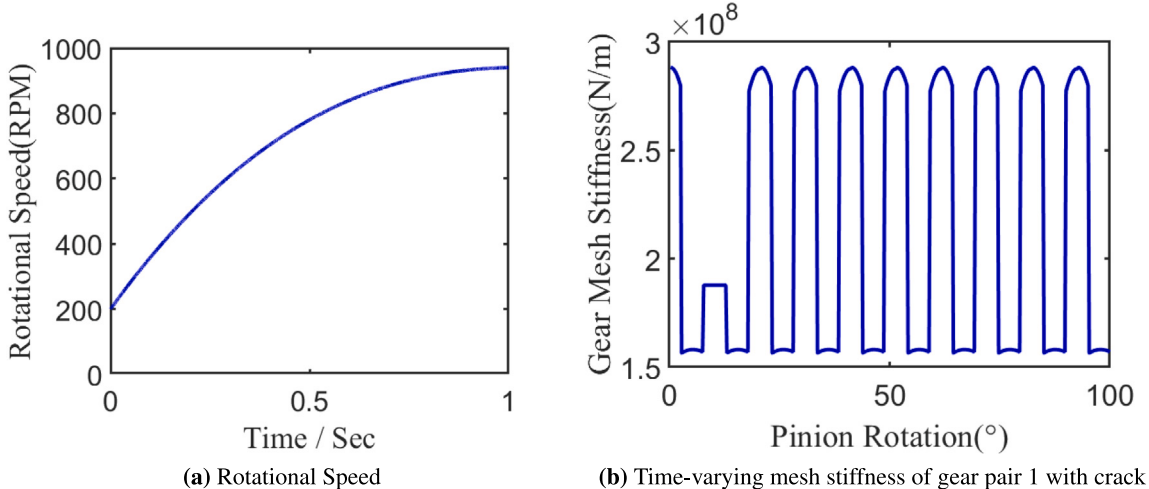


Fig. 4. The parameters of numerical example.

Next, the proposed method is used for evaluating the gear operating condition in simulation. Initially,  $\mathbf{F}$  is calculated in the frequency domain utilizing  $\mathbf{x}$  and  $\mathbf{H}^{\text{Decoup}}$ . The FRF matrix is derived from the virtual decoupling technology from Simulation 1. The weighted matrix  $\mathbf{W}$ , chosen in this instance based on Eq. (18), controls the degree of ill-conditioning of  $\mathbf{A} = (\mathbf{H}^{\text{Decoup}})^T(\mathbf{H}^{\text{Decoup}})$ . The weighted matrix was utilized and it decreased by approximately two orders of magnitude. After that,  $\mathbf{F}$  is reconstructed as shown in Eq. (21).

The time-frequency distribution of the bearing force signals under simulated gear healthy conditions is depicted in Fig. 7. Notably, the presence of a gear crack fault impacts the distribution of the non-linear chirp components of the bearing force. Given that the characteristic frequency orders are used as criteria for assessing the gear's operating condition [56], we applied order

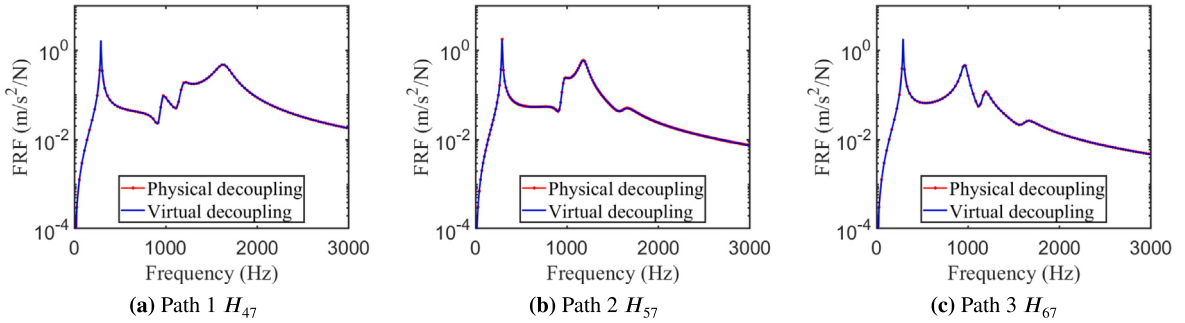


Fig. 5. Comparison of FRF between the physical decoupling and virtual decoupling.

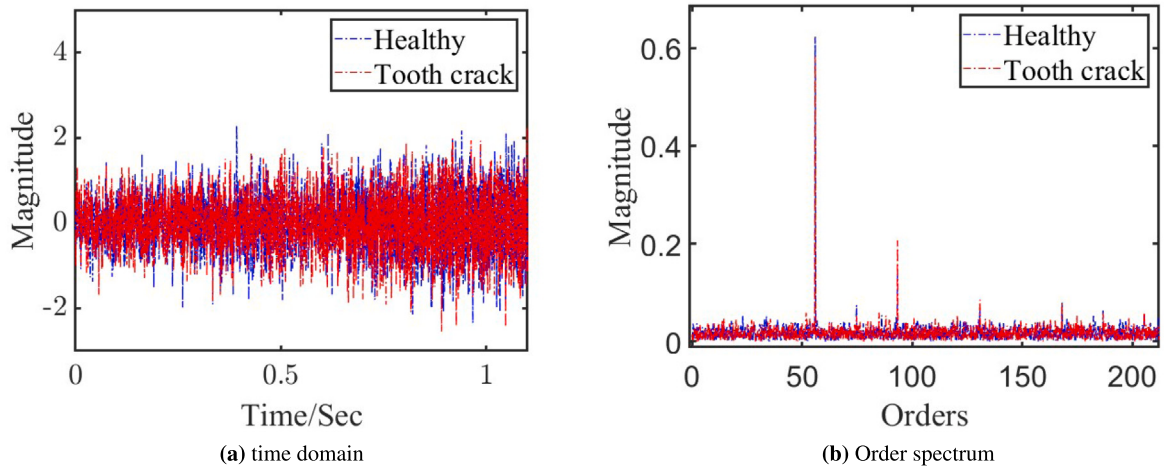


Fig. 6. Magnitude spectrum and order spectrum of simulated vibration signals.

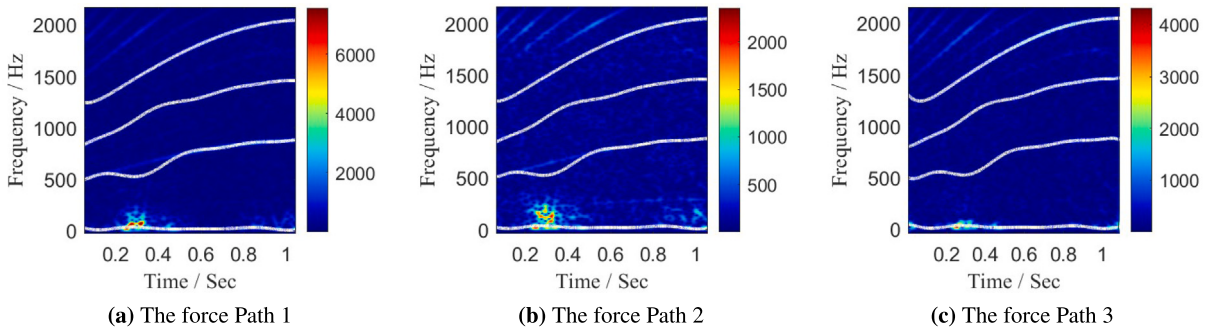


Fig. 7. Time–frequency distribution of VNCCD at three paths on the housing under gear healthy condition.

tracking to the bearing force signals for comparison. The order spectrum and characteristic frequency orders for the bearing force signals of Path 2, under both the gear cracking condition and the healthy condition, are presented in Fig. 8. By eliminating the intercoupling effect of structural vibration transfer paths, the order spectrum of the bearing force exhibits superior performance in fault diagnosis.

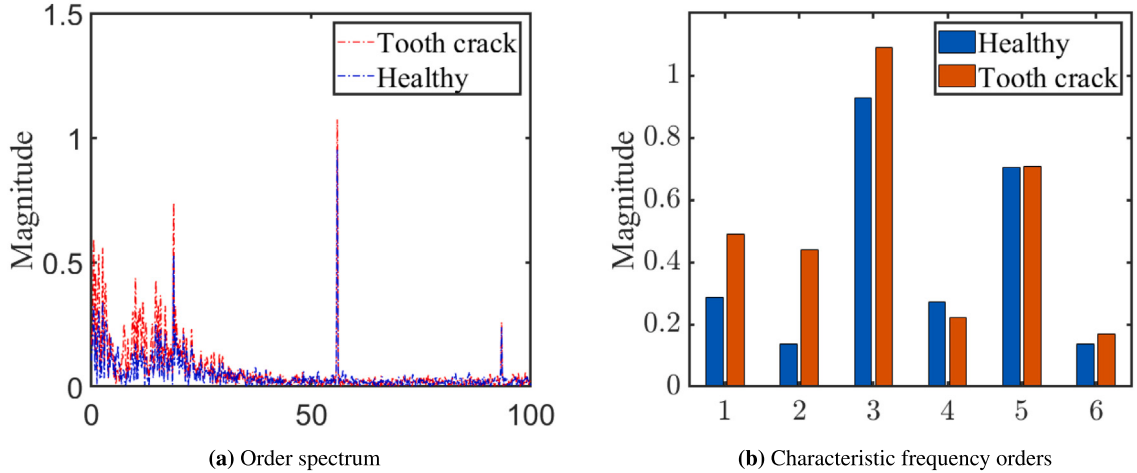


Fig. 8. Order spectrum and magnitude at characteristic frequency orders of bearing force signals.

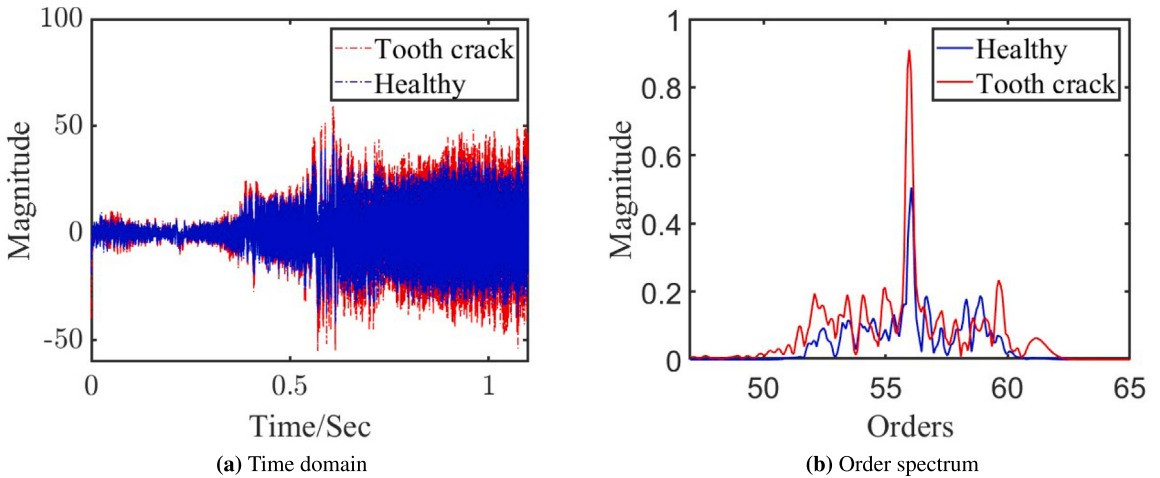


Fig. 9. VNCCD of bearing force of path 2.

**Table 1**  
The peak of the order spectrum of the VNCCD in numerical example.

	Path 1	Path 2	Path 3
Crack fault condition	3.3265	0.9102	0.8211
Health condition	3.1516	0.5055	0.6836
Increases	5.55%	80.0%	20.11%

In this case, the visual decoupled nonlinear chirp components is defined as the meshing frequency components and side-band frequency components. By way of illustration, we analyze the bearing dynamic force of Path 2. The reconstructed visual decoupled nonlinear chirp component signals in the time domain are presented in Fig. 9(a), while the order spectrum of the reconstructed visual decoupled nonlinear chirp component signal is displayed in Fig. 9(b). The maximum value in the order spectrum of the reconstructed visual decoupled nonlinear chirp component signal is indicated in Table 1. It is evident from Table 1 that the magnitudes of all visual decoupled nonlinear chirp components increase under the gear cracking condition.

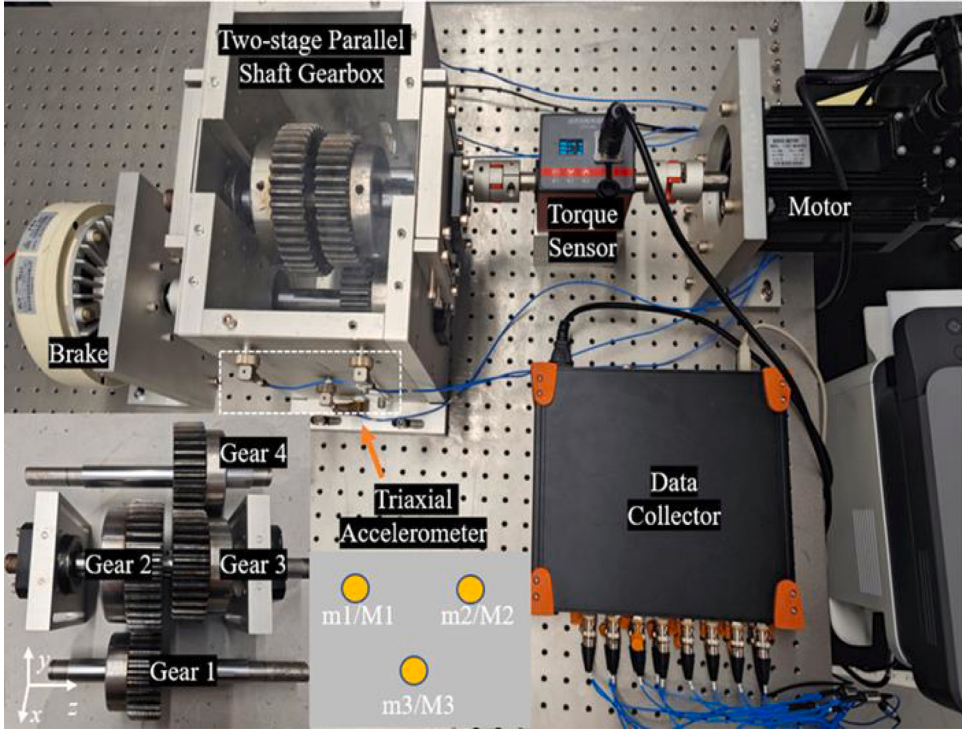


Fig. 10. The gearbox test rig in experiment.

**Table 2**  
Main parameters of the gear system in experimental.

Parameter	Value	Parameter	Value
Number of teeth	$Z_1 = 28, Z_2 = 40, Z_3 = 34, Z_4 = 34$	Density ( $\text{kg}/\text{m}^3$ )	7850
Young's modulus (GPa)	210	Radius of the shaft (mm)	24
Poisson's ratio	0.3	Module (mm)	3
Face width (mm)	16	Pressure angle ( $\circ$ )	20
Addendum coefficient	1	Bottom clearance coefficient	0.3

**Table 3**  
The test time of the virtual decoupling and physical decoupling.

	Dismantled	Hammer impact test	Assembled	Total
Virtual decoupling	–	60 (38 times)	–	60 min
Physical decoupling	100	20 (12 times)	90	210 min

## 5. Experimental verification

In this section of the paper, we demonstrate the effectiveness of this method through experiments. The two-stage gearbox test system used in the experiment is shown in Fig. 10. Table 2 lists the gear parameters. Vibration signals are measured with six triaxial accelerometers, the locations that are displayed in the illustration by yellow dots.

### 5.1. Decoupling transfer function via virtual decoupling

Six triaxial accelerometers are affixed to the gearbox housing. The gears are typically acceptable to neglect axial force [57]. In this study, only the  $x$  and  $y$  directions are considered in the model for transfer paths. To obtain the decoupled FRFs between passive part and measure point, the virtual decoupling method is employed, and an impact hammer (DH-LC02-3A105) is used for impulsive excitations. The data acquisition system (DH8303) records both excitation and response signals. Based on the frequency

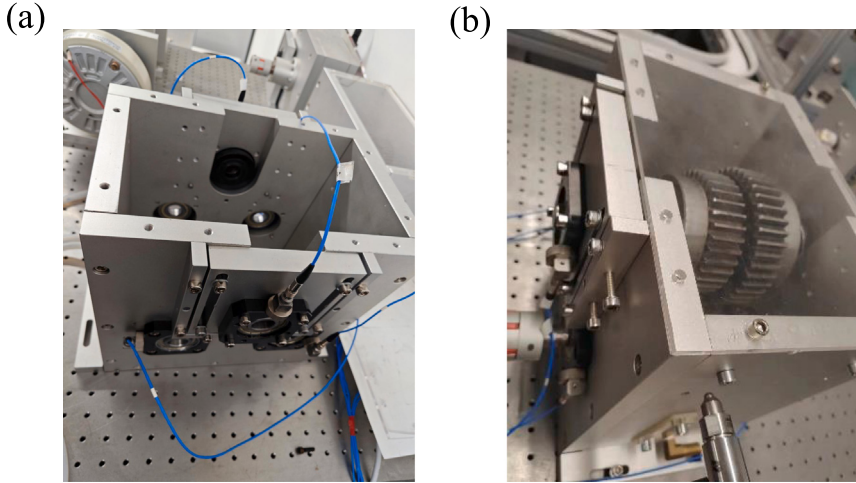


Fig. 11. FRF test: (a) physical decoupling; (b) virtual decoupling.

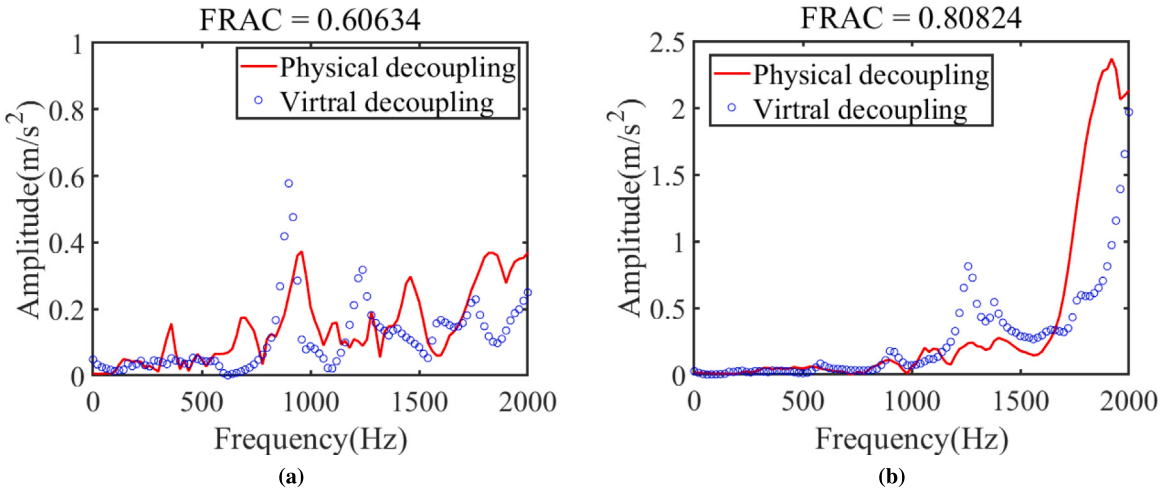


Fig. 12. FRFs obtained from virtual decoupling and physical decoupling: (a)  $H_{m1y4}$ ; (b)  $H_{m2y4}$

response curve obtained from the impact hammer, the frequency range of the excitation signal is constrained to below 5000 Hz. Consequently, the sampling frequency for the frequency response test is established at 8000 Hz. The effectiveness of the virtual decoupling method is compared against a physical decoupling test, which is considered the standard.

For the physical decoupling, disassembling all shafts and gears is required (as shown in Fig. 11(a)), but the virtual decoupling technology eliminates this need (as shown in Fig. 11(b)). The same six triaxial accelerometers are used in the FRF tests, enabling the acquisition of twelve FRFs from a single hammer test. To construct the full  $12 \times 12$  frequency response matrix (including components such as  $\mathbf{H}_{rr}^{coup}$ ,  $\mathbf{H}_{hr}^{coup}$ , and  $\mathbf{H}_{hh}^{coup}$ ), twelve hammer tests are needed.  $\mathbf{H}_{th}^{coup}$  is determined based on the reciprocity principle. Finally, acquiring the  $1 \times 12$  dimension matrix components ( $\mathbf{H}_{mr}^{coup}$  and  $\mathbf{H}_{mh}^{coup}$ ) requires only one hammer test.

A total of 38 hammer tests are required to collect the coupled FRFs. The virtual decoupling technique notably avoids assembly errors commonly associated with physical decoupling methods. By using the virtual decoupling method, the total test time can be reduced by 71% in this work. In Table 3, the time costs of each testing process are presented to quantify its efficiency. In Fig. 12, the decoupled FRFs, labeled  $H_{m1y4}$  and  $H_{m2y4}$ , are presented.

More specifically,  $H_{m1y4}$  represents the FRF that connects bearing 4 in the  $y$ -direction to measurement point 1. There is a significant correlation identified between the FRFs obtained by virtual decoupling techniques and physical decoupling techniques.

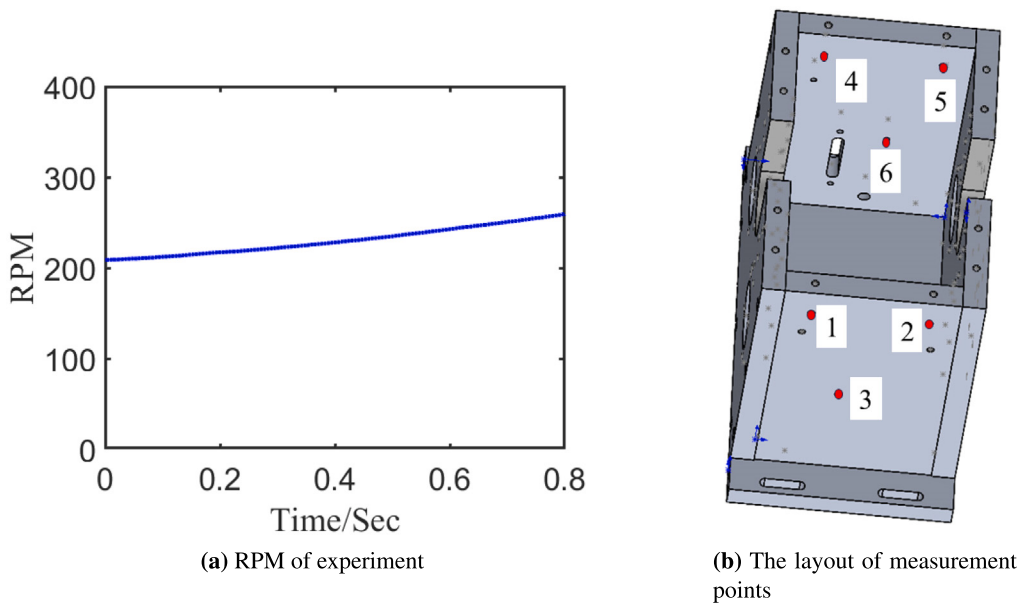


Fig. 13. Parameters of experiment under nonstationary

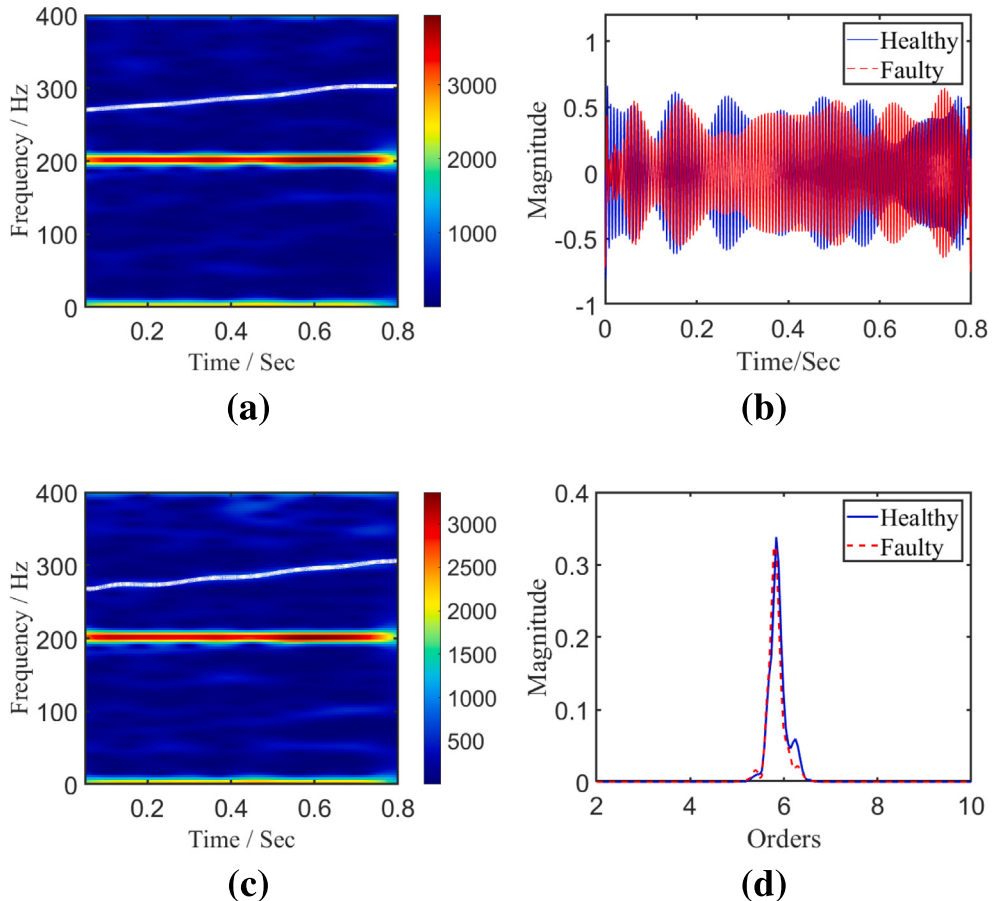
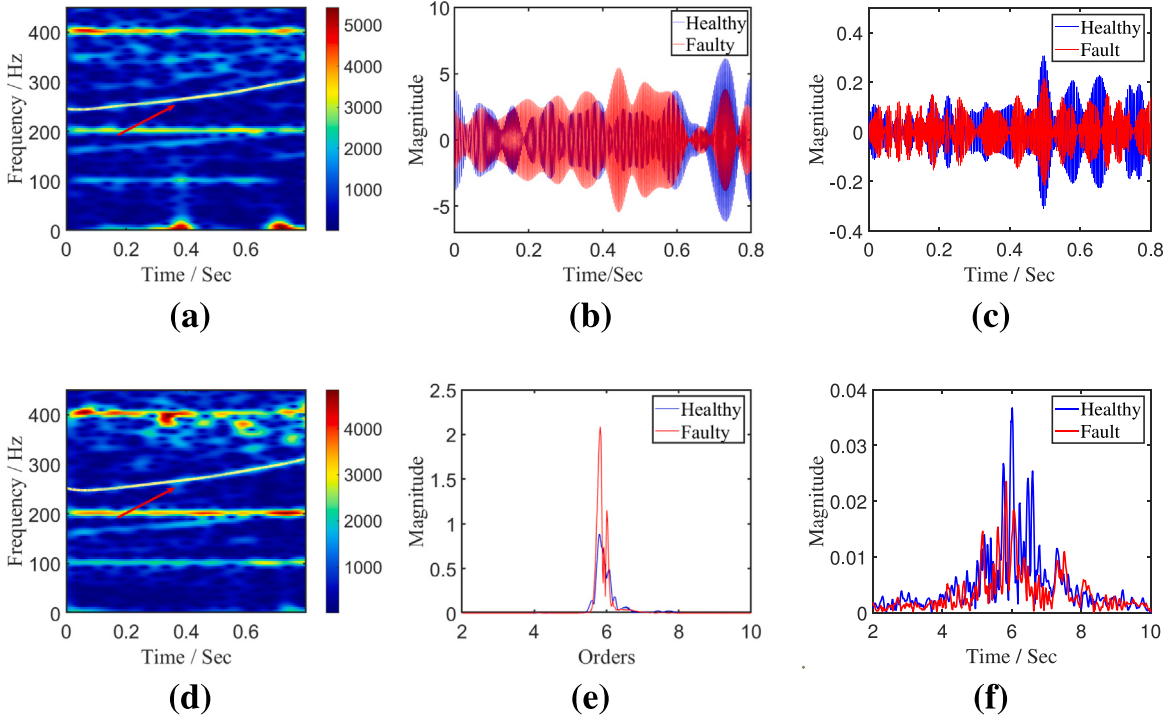


Fig. 14. Fault diagnosis based on vibration signal of 2x (a) Time–frequency image of vibration signals with faulty condition. (b) The extracted non-linear chirp components from vibration signals in time domain. (c) Time–frequency image of vibration signals with healthy condition. (d) Order spectrum of the nonlinear chirp components between healthy and faulty condition



**Fig. 15.** Fault diagnosis based on bearing dynamic force of path 3 (a) Time–frequency image of bearing force signals with faulty condition. (b) the reconstructed chirp component signal from bearing force signals by VNCCD. (c) the reconstructed chirp components' signal by SST2. (d) The time–frequency image of bearing force signals with healthy condition. (e) Order spectrum of the visual decoupled nonlinear chirp component signal by VNCCD. (e) Order spectrum of the reconstructed chirp component signal by SST2

The frequency response assurance criteria (FRAC) is used as an instrument to assess the level of similarity [58]:

$$\text{FRAC} = \frac{\left| \sum_{j=1}^{N_f} (\mathbf{H}_{\text{PD}}(\omega_j)^T \mathbf{H}_{\text{VD}}(\omega_j)) \right|^2}{\left[ \sum_{j=1}^{N_f} (\mathbf{H}_{\text{PD}}(\omega_j)^T \mathbf{H}_{\text{PD}}(\omega_j)) \right] \left[ \sum_{j=1}^{N_f} (\mathbf{H}_{\text{VD}}(\omega_j)^T \mathbf{H}_{\text{VD}}(\omega_j)) \right]} \quad (32)$$

Where the Hermitian transpose is denoted by the superscript T. The symbols VD and PD stand for the virtual decoupling and the physical decoupling, respectively. The discrete number is denoted by  $N_f$ .  $\omega$  represents the circular frequency. The FRAC of  $H_{m1y4}$  and  $H_{m2y4}$  is 0.60634 and 0.80824. This illustrates that the virtual decoupling approach is effective. In order to remove the effect of structural vibration paths and obtain the decoupled gearbox housing FRF, an alternative approach known as virtual decoupling has been introduced. Since the physical decoupling cannot be achieved in integrated gear systems, this technology assumes utmost importance.

## 5.2. Extracting force non-linear chirp components for fault diagnosis

In this subsection, the decoupled Frequency Response Function is employed to identify the bearing force signal of the gearbox operating under non-stationary conditions. The test rig undergoes a speed variation process, as illustrated in Fig. 13(a). Gear 2 on the transmission shaft is replaced. Consequently, bearing force and vibration are obtained under both healthy and gear 2 with a chipped tooth. The layout of measuring points for sensors is presented in Fig. 13(b). The sampling frequency during the experiment is set to 16000 Hz.

To effectively demonstrate the impacts of our proposed method, we initially utilize the original signal from the 2x measure point for fault diagnosis. The original signal under variety condition can be obtain these time–frequency image by GPTF. Fig. 14(a) and Fig. 14(c) show the comparison of time–frequency images between the vibration signals from the gear with a chipped tooth fault and those from the healthy condition. Fig. 14(b) displays the reconstructed non-chirp components from the original vibration signals in the time domain, with the non-chirp components extracted from the x signal. It is challenging to distinguish between the conditions of the various gears. Similarly, we apply the order tracking technology to the reconstructed non-chirp components for fault diagnosis. As shown in Fig. 14(d), order tracking struggles to determine the health of the gear, primarily due to the influence of the structural transfer paths on the characteristics of the vibration signal.

**Table 4**  
The peak of the order spectrum the reconstructed VNCCD signals.

	1X	1Y	2X	2Y	3X	3Y
Fault condition	3.5407	5.8604	2.0703	29.7496	7.1463	5.4908
Health condition	0.7364	1.2388	1.0609	8.5676	5.6154	4.3110
Increases	380.8%	373.1%	95.1%	247.2%	27.2%	27.3%
	<b>4X</b>	<b>4Y</b>	<b>5X</b>	<b>5Y</b>	<b>6X</b>	<b>6Y</b>
Fault condition	8.9245	7.5003	7.5437	7.5549	13.2318	1.9345
Health condition	3.9293	1.8206	3.3931	2.3264	5.3513	1.3733
Increases	127.1%	312.0%	122.3%	224.7%	147.2%	40.8%

Subsequently, the MWI is applied to identify the bearing dynamic forces of the gearbox. By utilizing the measured vibration response signals  $x$  and the decoupled FRF  $H_{mh}$ , the bearing force signals are identified. Moreover, the vibration signals from accelerometers 1, 2, and 3 are employed, with data from these three measured points used to solve the dynamic inverse problem.

Similarly, let us consider the case of a bearing dynamic force 2x. The time-frequency distribution estimated using GPTF with fitted IFs under the gear faulty conditions and the healthy conditions are presented in Fig. 15(a) and Fig. 15(d), respectively. The red arrow points to the chirp component that is extracted and reconstructed directly from the bearing force signal. The reconstructed visual decoupled nonlinear chirp component signal in the time domain is illustrated in Fig. 15(b), while the order spectrum of the reconstructed visual decoupled nonlinear chirp component signal is depicted in Fig. 15(e). As Second-order Synchrosqueezing Transform(SST2) is an existing technique known for its high efficiency in extracting time-frequency features, we have used it for comparative experiments [59]. The results of this algorithm are presented in Fig. 15(c) and Fig. 15(f). The comparative experiments demonstrate the efficiency of our algorithm Table 4 showcases the distinctiveness of the features extracted by the VNCCD method under different conditions. This phenomenon demonstrates the effectiveness of the proposed method in mitigating the coupling effect of the structural transfer path and enhancing the quality of the signal. When compared to the vibration signal, the extracted VNCCDs exhibit improved efficacy in diagnosing gearbox faults.

## 6. Conclusions

This study presents a novel technique, called the VNCCD method, for diagnosing faults in gear systems under nonstationary conditions. A transfer path model of the gear system is established, and virtual decoupling technology is introduced to obtain the frequency response function without disassembly. The bearing force is identified in the frequency domain based on the resulting frequency response function. By employing the IFT and a signal decomposition technique, nonlinear chirp components are successfully extracted. The VNCCD effectively demonstrates the phenomenon of magnitude increase compared to the inherent nonlinear chirp component from the original signal. Experimental research and simulations provide substantial evidence of the proposed approach's efficacy in diagnosing gear faults. However, our study still has the following drawbacks:

- The transfer path function of the gearbox is typically a nonlinear time-varying function, but we modeled it as a linear time-invariant function, which has low accuracy requirements.
- The time-frequency feature extraction algorithm based on ridges requires a high-quality initial ridge; an inappropriate initial ridge can lead to erroneous results.

To address these issues, our future research will focus on the mechanical properties of the gearbox and more robust time-frequency feature extraction algorithms.

## CRediT authorship contribution statement

**Cai Li:** Writing – original draft, Validation, Methodology, Conceptualization. **Penghong Lu:** Validation, Methodology. **Gang Chen:** Writing – review & editing, Validation, Supervision, Resources, Funding acquisition, Formal analysis.

## Declaration of competing interest

The authors declare that they have no known competing financial interests or personal relationships that could have appeared to influence the work reported in this paper.

## Data availability

Data will be made available on request.

## Acknowledgments

This work is partially supported the National Science Foundation of China (Grant No. 52305105), the Basic and Applied Basic Research Foundation of Guangdong Province, China (Grant No. 2022A1515240027 and No. 2023A1515010812), and the Basic and Applied Basic Research Foundation of Guangzhou, China (Grant No. 2023A04J1582).

**Table 5**  
Main parameters of the numerical example.

Parameters	Value	Parameters	Value
Number of teeth	$Z_1 = 28, Z_2 = 40, Z_3 = 34, Z_4 = 34$	(kg/m <sup>3</sup> )	7850
Young's modulus (GPa)	210	Radius of the shaft (mm)	24
Poisson's ratio	0.3	Module (mm)	3
Face width (mm)	16	Pressure angle ( $\circ$ )	20
Addendum coefficient	1	Bottom clearance coefficient	0.3
Mass (kg)	$M_4 = 1, M_5 = 2, M_3 = 3, M_7 = 23.5$	Damping ratio	0.02
Damp(N s/m)	$c_{36} = 1e4, c_{25} = 1e4, c_{14} = 1e4$	Stiffness (N/m)	$k_{36} = 1e7, k_{25} = 1e7$
Damp(N s/m)	$c_{47} = 1e3, c_{57} = 1e3, c_{67} = 1e3$	Stiffness (N/m)	$k_{14} = 1e7$
			$k_{47} = 1e8, k_{57} = 1e8$
			$k_{67} = 1e8$

## Appendix A. Detailed parameters of the numerical example

The differential equation of the lumped parameter model is as follow:

$$\mathbf{M}\ddot{\mathbf{q}} + \mathbf{C}\dot{\mathbf{q}} + \mathbf{K}\mathbf{q} = \mathbf{G} \quad (\text{A.1})$$

Where the symbols  $\mathbf{M}$ ,  $\mathbf{C}$  and  $\mathbf{K}$  stand for the mass matrix, the damping matrix and the stiffness of the lumped model, respectively. The Table 5 lists the specific parameters.  $\mathbf{q}$  and  $\mathbf{G}$  represents the generalized coordinate vector and the generalized force. The generalized coordinate vector of lumped parameter model is as follows:

$$\mathbf{q} = [x_1 \ \theta_1 \ x_2 \ \theta_2 \ x_3 \ \theta_3 \ x_4 \ x_5 \ x_6 \ x_7] \quad (\text{A.2})$$

Where  $x_i$  and  $\theta_i$  stand for the linear and angular displacement of  $i$ th part of the lumped model, respectively. The global mass matrix of the model is:

$$\mathbf{M}^{coup} = \text{diag}(m_1 \ J_1 \ m_2 \ J_2 \ m_3 \ J_3 \ m_4 \ m_5 \ m_6 \ m_7) \quad (\text{A.3})$$

Where  $m_i$  and  $J_i$  stand for the mass and moment of inertia of the  $i$ th part of the lumped model, respectively.

The FRFs of the total system is as follows:

$$\mathbf{H}^{coup} = \omega^2(-\omega^2\mathbf{M}^{coup} + j\omega\mathbf{C}^{coup} + \mathbf{C}^{coup})^{-1} \quad (\text{A.4})$$

The time-varying damping and stiffness matrices of the coupled system are denoted by  $\mathbf{C}^{coup}$  and  $\mathbf{K}^{coup}$ , respectively. The mass matrix of the passive part is as follows:

$$\mathbf{M}^{Decoup} = \text{diag}(m_4 \ m_5 \ m_6 \ m_7) \quad (\text{A.5})$$

For the passive part, the stiffness matrix is:

$$\mathbf{K}^{Decoup} = \begin{bmatrix} k_{47} & 0 & 0 & -k_{47} \\ 0 & k_{57} & 0 & -k_{57} \\ 0 & 0 & k_{67} & -k_{67} \\ -k_{47} & -k_{57} & -k_{67} & k_{47}+k_{57}+k_{67}+k_{07} \end{bmatrix} \quad (\text{A.6})$$

For the passive part, the damping matrix is:

$$\mathbf{C}^{Decoup} = \begin{bmatrix} c_{47} & 0 & 0 & -c_{47} \\ 0 & c_{57} & 0 & -c_{57} \\ 0 & 0 & c_{67} & -c_{67} \\ -c_{47} & -c_{57} & -c_{67} & c_{47}+c_{57}+c_{67}+c_{07} \end{bmatrix} \quad (\text{A.7})$$

For the passive part, The theoretical decoupled FRFs can be obtained as:

$$\mathbf{H}^{Decoup} = \omega^2(-\omega^2\mathbf{M}^{Decoup} + j\omega\mathbf{C}^{Decoup} + \mathbf{K}^{Decoup})^{-1} \quad (\text{A.8})$$

The global stiffness matrix of the gear system is  $\mathbf{K}^{coup} = [K_1^{coup}, K_2^{coup}]$ , where

$$K_1^{coup} = \begin{bmatrix} k_{14}+k_1(t) & r_{b1}k_1(t) & -k_1(t) & r_{b2}k_1(t) & 0 \\ r_{b1}k_1(t) & r_{b1}^2k_1(t) & -r_{b1}k_1(t) & r_{b1}r_{b2}k_1(t) & 0 \\ -k_1(t) & r_{b1}k_1(t) & k_1(t)+k_2(t) & -r_{b2}k_1(t)+r_{b3}k_2(t) & -k_2(t) \\ r_{b2}k_1(t) & r_{b1}r_{b2}k_1(t) & -r_{b1}k_2(t)+r_{b3}k_2(t) & r_{b2}^2k_1(t)+r_{b3}^2k_2(t) & -r_{b3}k_2(t) \\ 0 & 0 & -k_2(t) & -r_{b3}k_2(t) & k_2(t) \\ 0 & 0 & r_{b4}k_2(t) & r_{b3}r_{b4}k_2(t) & -r_{b4}k_2(t) \\ -k_{14} & 0 & 0 & 0 & 0 \\ 0 & 0 & -k_{25} & 0 & 0 \\ 0 & 0 & 0 & 0 & -k_{36} \\ 0 & 0 & 0 & 0 & 0 \end{bmatrix} \quad (\text{A.9})$$

$$K_2^{coup} = \begin{bmatrix} 0 & -k_{14} & 0 & 0 & 0 \\ 0 & 0 & 0 & 0 & 0 \\ -k_2(t) & r_{b4}k_2(t) & 0 & -k_{25} & 0 \\ r_{b3}r_{b4}k_2(t) & 0 & 0 & 0 & 0 \\ -r_{b4}k_2(t) & 0 & 0 & -k_{36} & 0 \\ r_{b4}^2k_2(t) & 0 & 0 & 0 & 0 \\ 0 & k_{14} + k_{47} & 0 & 0 & -k_{47} \\ 0 & 0 & k_{25} + k_{57} & 0 & -k_{57} \\ 0 & 0 & 0 & k_{36} + k_{67} & -k_{67} \\ 0 & -k_{47} & -k_{57} & -k_{67} & k_{47} + k_{57} + k_{67} + k_{07} \end{bmatrix} \quad (\text{A.10})$$

where  $k_{ij}$  is the stiffness between part  $i$  and  $j$ .  $r_{bi}$  stands for base radius of  $i$ th gear.  $k_i(t)$  represents the time-variable meshing stiffness of gear pair  $i$  (see Table 5). The global damp matrix of the gear system is  $\mathbf{C}^{coup} = [C_1^{coup}, C_2^{coup}]$ , where

$$C_1^{coup} = \begin{bmatrix} c_{14} + c_1(t) & r_{b1}c_1(t) & -c_1(t) & r_{b2}c_1(t) & 0 \\ r_{b1}c_1(t) & r_{b1}^2c_1(t) & -r_{b1}c_1(t) & r_{b1}r_{b2}c_1(t) & 0 \\ -c_1(t) & r_{b1}c_1(t) & c_1(t) + c_2(t) & -r_{b2}c_1(t) + r_{b3}c_2(t) & -c_2(t) \\ r_{b2}c(t) & r_{b1}r_{b2}c_1(t) & -r_{b1}c_2(t) + r_{b3}c_2(t) & r_{b2}^2c_1(t) + r_{b3}^2c_2(t) & -r_{b3}c_2(t) \\ 0 & 0 & -c_2(t) & -r_{b3}c_2(t) & c_2(t) \\ 0 & 0 & r_{b4}c_2(t) & r_{b3}r_{b4}c_2(t) & -r_{b4}c_2(t) \\ -c_{14} & 0 & 0 & 0 & 0 \\ 0 & 0 & -c_{25} & 0 & 0 \\ 0 & 0 & 0 & 0 & -c_{36} \\ 0 & 0 & 0 & 0 & 0 \end{bmatrix} \quad (\text{A.11})$$

$$C_2^{coup} = \begin{bmatrix} 0 & -c_{14} & 0 & 0 & 0 \\ 0 & 0 & 0 & 0 & 0 \\ r_{b4}c_2(t) & 0 & -c_{25} & 0 & 0 \\ r_{b3}r_{b4}c_2(t) & 0 & 0 & 0 & 0 \\ -r_{b4}c_2(t) & 0 & 0 & -c_{36} & 0 \\ r_{b4}^2c_2(t) & 0 & 0 & 0 & 0 \\ 0 & c_{14} + c_{47} & 0 & 0 & -c_{47} \\ 0 & 0 & c_{25} + c_{57} & 0 & -c_{57} \\ 0 & 0 & 0 & c_{36} + c_{67} & -c_{67} \\ 0 & -c_{47} & -c_{57} & -c_{67} & c_{47} + c_{57} + c_{67} + c_{07} \end{bmatrix} \quad (\text{A.12})$$

where  $c_{ij}$  is the stiffness between part  $i$  and  $j$ .  $c_i(t)$  represents the time-variable meshing stiffness of gear pair  $i$ .

## Appendix B. Bearing dynamic force estimation

In this section, we introduce the algorithm for identifying bearing forces and briefly demonstrate the concept of this algorithm. The proof of the consistency and unbiasedness of the algorithm can be found in [47], which is shown in Table 6. Note that we omit the scripts of “Decoup” and “mh” to focus on the algorithm itself.

**Lemma ([60]).** The least upper bound of the raw matrix is  $\frac{\delta \mathbf{f}}{\mathbf{F}} \leq k(\tilde{\mathbf{A}}) \frac{\|\mathbf{A}\| \|\delta \mathbf{y}\|}{\|\mathbf{A}\| \|\mathbf{y}\|} + k(\tilde{\mathbf{A}}) \frac{\|\delta \mathbf{A}\|}{\|\mathbf{A}\|}$ , where  $k(\tilde{\mathbf{A}}) = \|\tilde{\mathbf{A}}\| \|\tilde{\mathbf{A}}^\dagger\|$ ,  $\mathbf{A} = \mathbf{H}^T \mathbf{H}$  and  $\mathbf{y} = \mathbf{H}^T \mathbf{x}$  in (13). The symbol  $\delta$  and  $\|\cdot\|$  stands for error and Frobenius norm of matrix.

**Corollary.** The least upper bound of the with weighted matrix is  $\frac{\delta \mathbf{f}}{\mathbf{f}} \leq k(\tilde{\mathbf{A}} \mathbf{W}) \frac{\|\mathbf{A}\| \|\mathbf{W}\| \|\delta \mathbf{y}\|}{\|\mathbf{A} \mathbf{W}\| \|\mathbf{y}\|} + k(\tilde{\mathbf{A}} \mathbf{W}) \frac{\|\delta \mathbf{A} \mathbf{W}\|}{\|\tilde{\mathbf{A}} \mathbf{W}\|}$  where  $k(\tilde{\mathbf{A}} \mathbf{W})$  stands for the condition number of  $\tilde{\mathbf{A}} \mathbf{W}$ .

**Proof.** We use Lemma to analysis the Eq. (14):

$$\frac{\delta \mathbf{f}}{\mathbf{f}} \leq k(\tilde{\mathbf{A}} \mathbf{W}) \frac{\|\mathbf{A} \mathbf{W}\| \|\delta \mathbf{y}\|}{\|\mathbf{A} \mathbf{W}\| \|\mathbf{y}\|} + k(\tilde{\mathbf{A}} \mathbf{W}) \frac{\|\delta \mathbf{A} \mathbf{W}\|}{\|\tilde{\mathbf{A}} \mathbf{W}\|} \quad (\text{B.13})$$

Due to  $\|\mathbf{A} \mathbf{W}\| \leq \|\mathbf{A}\| \|\mathbf{W}\|$ , the equation can be written as:

$$\frac{\delta \mathbf{f}}{\mathbf{f}} \leq k(\tilde{\mathbf{A}} \mathbf{W}) \frac{\|\mathbf{A}\| \|\mathbf{W}\| \|\delta \mathbf{y}\|}{\|\mathbf{A} \mathbf{W}\| \|\mathbf{y}\|} + k(\tilde{\mathbf{A}} \mathbf{W}) \frac{\|\delta \mathbf{A} \mathbf{W}\|}{\|\tilde{\mathbf{A}} \mathbf{W}\|} \quad (\text{B.14})$$

The proof is finished.

The purpose of the weighting matrix is to reduce the upper bound of the correlation error, the following is constrained:

$$k(\tilde{\mathbf{A}} \mathbf{W}) \frac{\|\mathbf{A}\| \|\mathbf{W}\|}{\|\tilde{\mathbf{A}} \mathbf{W}\|} \leq k(\tilde{\mathbf{A}}) \frac{\|\mathbf{A}\|}{\|\tilde{\mathbf{A}}\|}, \quad k(\tilde{\mathbf{A}} \mathbf{W}) \frac{\|\delta \mathbf{A} \mathbf{W}\|}{\|\tilde{\mathbf{A}} \mathbf{W}\|} \leq k(\tilde{\mathbf{A}}) \frac{\|\mathbf{A}\|}{\|\tilde{\mathbf{A}}\|} \quad (\text{B.15})$$

**Table 6**  
Bearing dynamic force estimation.

---

```

1: Initialize:  $\mathbf{f}^{(0)} \leftarrow 0, \mathbf{W}^{(0)} \leftarrow I, r \leftarrow 0, k \leftarrow 1, x, \mathbf{H}, \varepsilon$ 
2: while  $k(\mathbf{H}^T \mathbf{H} \mathbf{W}^{(0)} \dots \mathbf{W}^{(r+1)}) \leq k(\mathbf{H}^T \mathbf{H} \mathbf{W}^{(0)} \dots \mathbf{W}^{(r)})$ 
   3: Compute  $\mathbf{W}^{(r+1)}$  for matrix  $\mathbf{A}$ 
   4:  $\mathbf{H}^T \mathbf{H} \mathbf{W}^{(0)} \dots \mathbf{W}^{(r)} \leftarrow \mathbf{H}^T \mathbf{H} \mathbf{W}^{(0)} \dots \mathbf{W}^{(r+1)}$ 
   5:  $r \leftarrow r + 1$ , end while
   6:  $\alpha \leftarrow$  obtain the value through GCV
7:  $\mathbf{f}^{(1)} \leftarrow$  Solve  $(\mathbf{H}^T \mathbf{H} \mathbf{W}^{(0)} \dots \mathbf{W}^{(r)} + \alpha \mathbf{I}) \mathbf{f}^{(1)} = \mathbf{H}^T \mathbf{x} + \alpha \mathbf{f}^{(0)}$  by LU Decomposition.
8: while  $\frac{\|\mathbf{e}^{(k)}\|}{\|\mathbf{f}^{(k)}\|} \geq \varepsilon$ 
   9:  $r^k \leftarrow \mathbf{H}^T \mathbf{x} - \mathbf{H}^T \mathbf{H} \mathbf{W}^{(0)} \dots \mathbf{W}^{(r)} \mathbf{f}^{(k)}$ 
  10:  $\mathbf{e}^{(k)} \leftarrow$  Solve  $(\mathbf{H}^T \mathbf{H} \mathbf{W}^{(1)} \dots \mathbf{W}^{(r)} + \alpha \mathbf{I}) \mathbf{e}^{(k)} = r^k$  by LU Decomposition.
  11:  $\mathbf{f}^{(k+1)} \leftarrow \mathbf{f}^{(k)} + \mathbf{e}^{(k)}, k + 1 \leftarrow k + 1$ 
12: end while
13:  $F \leftarrow \mathbf{W}^{(1)} \dots \mathbf{W}^{(r)} \mathbf{f}^{(k)}$ 

```

---

Considering  $\|\tilde{\mathbf{A}}\mathbf{W}\| \leq \|\tilde{\mathbf{A}}\| \|\mathbf{W}\|$ , the above constraints are modified to:

$$k(\tilde{\mathbf{A}}\mathbf{W}) \leq k(\tilde{\mathbf{A}}), \quad \|\tilde{\mathbf{A}}\| \|\mathbf{W}\| = \|\tilde{\mathbf{A}}\mathbf{W}\| \text{ and } \frac{\|\delta \mathbf{A}\mathbf{W}\|}{\|\tilde{\mathbf{A}}\mathbf{W}\|} \leq \frac{\|\delta \mathbf{A}\|}{\|\tilde{\mathbf{A}}\|} \quad (\text{B.16})$$

For the above formula, we can obtain  $\frac{\|\delta \mathbf{A}\mathbf{W}\|}{\|\tilde{\mathbf{A}}\mathbf{W}\|} = \frac{\|\delta \mathbf{A}\mathbf{W}\|}{\|\mathbf{A}\| \|\mathbf{W}\|} \leq \frac{\|\delta \mathbf{A}\| \|\mathbf{W}\|}{\|\mathbf{A}\| \|\mathbf{W}\|} = \frac{\|\delta \mathbf{A}\|}{\|\mathbf{A}\|}$  and  $k(\tilde{\mathbf{A}}\mathbf{W}) \frac{\|\mathbf{A}\| \|\mathbf{W}\|}{\|\tilde{\mathbf{A}}\mathbf{W}\|} = k(\tilde{\mathbf{A}}\mathbf{W}) \frac{\|\mathbf{A}\| \|\mathbf{W}\|}{\|\mathbf{A}\| \|\mathbf{W}\|} \leq k(\tilde{\mathbf{A}}) \frac{\|\mathbf{A}\|}{\|\mathbf{A}\|}$ . Obviously, the three constraints will hold if the second constraint is satisfied.

The weighted matrix  $\mathbf{W}$  can be written:

$$\mathbf{W} = \text{diag}(w_1, w_2, \dots, w_m), w_k = \sqrt{\frac{\sum_{i=1}^m a_{ik}^2}{\sum_{i=1, j=1}^{m, m} a_{ij}^2}} \quad (\text{B.17})$$

When the weighted matrix  $\mathbf{W}$  is introduced:

$$\begin{aligned} \|\tilde{\mathbf{A}}\|_F \|\mathbf{W}\|_F &= \sqrt{\sum_{i=1}^m a_{i1}^2 + \sum_{i=1}^m a_{i2}^2 + \dots + \sum_{i=1}^m a_{im}^2} \sqrt{w_1^2 + w_2^2 + \dots + w_n^2} \\ &\geq \sqrt{w_1^2 \sum_{i=1}^m a_{i1}^2 + w_2^2 \sum_{i=1}^m a_{i2}^2 + \dots + w_m^2 \sum_{i=1}^m a_{im}^2} \\ &= \sqrt{\sum_{i=1}^m w_i^2 a_{i1}^2 + \sum_{i=1}^m w_i^2 a_{i2}^2 + \dots + \sum_{i=1}^m w_i^2 a_{im}^2} = \|\tilde{\mathbf{A}}\mathbf{W}\|_F \end{aligned}$$

Due to the Cauchy Inequality,  $\frac{\sum_{i=1}^m a_{i1}^2}{w_1^2} = \frac{\sum_{i=1}^m a_{i2}^2}{w_2^2} = \dots = \frac{\sum_{i=1}^m a_{im}^2}{w_m^2} = \sum_{i=1, j=1}^{m, m} a_{ij}^2 = c$ , the second constraint does hold.

## References

- [1] Xiannian Kong, Zehua Hu, Jinyuan Tang, Siyu Chen, Zhiwei Wang, Effects of gear flexibility on the dynamic characteristics of spur and helical gear system, *Mech. Syst. Signal Process.* 184 (2023) 109691.
- [2] Zimeng Liu, Erliang Shang, Yifan Huangfu, Hui Ma, Jiazen Zhu, Songtao Zhao, Xinhua Long, Zhanwei Li, Vibration characteristics analysis of flexible helical gear system with multi-tooth spalling fault: Simulation and experimental study, *Mech. Syst. Signal Process.* 201 (2023) 110687.
- [3] Xiao Yang, Yaguo Lei, Huan Liu, Bin Yang, Xiang Li, Naipeng Li, Rigid-flexible coupled modeling of compound multistage gear system considering flexibility of shaft and gear elastic deformation, *Mech. Syst. Signal Process.* 200 (2023) 110632.
- [4] Yi Yang, Niaoqing Hu, Yuehao Li, Zhe Cheng, Guoji Shen, Dynamic modeling and analysis of planetary gear system for tooth fault diagnosis, *Mech. Syst. Signal Process.* 207 (2024) 110946.
- [5] Ke Feng, J.C. Ji, Qing Ni, Michael Beer, A review of vibration-based gear wear monitoring and prediction techniques, *Mech. Syst. Signal Process.* 182 (2023) 109605.
- [6] Peng Zhou, Shiqian Chen, Qingbo He, Dong Wang, Zhike Peng, Rotating machinery fault-induced vibration signal modulation effects: A review with mechanisms, extraction methods and applications for diagnosis, *Mech. Syst. Signal Process.* 200 (2023) 110489.
- [7] Mantang Hu, Guofeng Wang, Kaile Ma, Identification of wind turbine gearbox weak compound fault based on optimal empirical wavelet transform, *Meas. Sci. Technol.* 34 (4) (2023) 045003.
- [8] Amir Eshghai Chaleshtori, Abdollah Aghaie, A novel bearing fault diagnosis approach using the gaussian mixture model and the weighted principal component analysis, *Reliab. Eng. Syst. Saf.* 242 (2024) 109720.
- [9] Yifan Li, Xin Zhang, Zaigang Chen, Yaocheng Yang, Changqing Geng, Ming J Zuo, Time-frequency ridge estimation: An effective tool for gear and bearing fault diagnosis at time-varying speeds, *Mech. Syst. Signal Process.* 189 (2023) 110108.
- [10] Sai Ma, Qinkai Han, Fulei Chu, Sparse representation learning for fault feature extraction and diagnosis of rotating machinery, *Expert Syst. Appl.* 232 (2023) 120858.

- [11] Yi Liu, Hang Xiang, Zhansi Jiang, Jiawei Xiang, Refining the time-frequency characteristic of non-stationary signal for improving time-frequency representation under variable speeds, *Sci. Rep.* 13 (1) (2023) 5215.
- [12] Xiaohui Duan, Zhipeng Feng, Time-varying filtering for nonstationary signal analysis of rotating machinery: Principle and applications, *Mech. Syst. Signal Process.* 192 (2023) 110204.
- [13] Shiqian Chen, Xingjian Dong, Zhike Peng, Wenming Zhang, Guang Meng, Nonlinear chirp mode decomposition: A variational method, *IEEE Trans. Signal Process.* 65 (22) (2017) 6024–6037.
- [14] Shiqian Chen, Yang Yang, Zhike Peng, Xingjian Dong, Wenming Zhang, Guang Meng, Adaptive chirp mode pursuit: Algorithm and applications, *Mech. Syst. Signal Process.* 116 (2019) 566–584.
- [15] Shiqian Chen, Minggang Du, Zhike Peng, Zhipeng Feng, Wenming Zhang, Fault diagnosis of planetary gearbox under variable-speed conditions using an improved adaptive chirp mode decomposition, *J. Sound Vib.* 468 (2020) 115065.
- [16] Shiqian Chen, Xingjian Dong, Guanpei Xing, Zhike Peng, Wenming Zhang, Guang Meng, Separation of overlapped non-stationary signals by ridge path regrouping and intrinsic chirp component decomposition, *IEEE Sens. J.* 17 (18) (2017) 5994–6005.
- [17] Siliang Lu, Ruqiang Yan, Yongbin Liu, Qunjing Wang, Tacholess speed estimation in order tracking: A review with application to rotating machine fault diagnosis, *IEEE Trans. Instrum. Meas.* 68 (7) (2019) 2315–2332.
- [18] Qixiang Zhang, Rui Yuan, Yong Lv, Zhaolun Li, Hongan Wu, Multivariate dynamic mode decomposition and its application to bearing fault diagnosis, *IEEE Sens. J.* 23 (7) (2023) 7514–7524.
- [19] Zhenling Mo, Heng Zhang, Yong Shen, Jianyu Wang, Hongyong Fu, Qiang Miao, Conditional empirical wavelet transform with modified ratio of cyclic content for bearing fault diagnosis, *ISA Trans.* 133 (2023) 597–611.
- [20] Xihui Liang, Ming J. Zuo, Zhipeng Feng, Dynamic modeling of gearbox faults: A review, *Mech. Syst. Signal Process.* 98 (2018) 852–876.
- [21] Daniel Jung, Yi Dong, Erik Frisk, Mattias Krysander, Gautam Biswas, Sensor selection for fault diagnosis in uncertain systems, *Int. J. Control* 93 (3) (2020) 629–639.
- [22] Yi Tan, Limao Zhang, Computational methodologies for optimal sensor placement in structural health monitoring: a review, *Struct. Health Monit.* 19 (4) (2020) 1287–1308.
- [23] Wenbing Tu, Jinwen Yang, Ya Luo, Lianbao Jiang, Jin Xu, Wennian Yu, et al., Vibration transmission characteristics and measuring points analysis of bearing housing system, *Shock Vib.* 2022 (2022).
- [24] Tulay Ercan, Omid Sedehi, Lambros S Katafygiotis, Costas Papadimitriou, Information theoretic-based optimal sensor placement for virtual sensing using augmented kalman filtering, *Mech. Syst. Signal Process.* 188 (2023) 110031.
- [25] D. De Domenico, G. Ricciardi, Dynamic response of non-classically damped structures via reduced-order complex modal analysis: Two novel truncation measures, *J. Sound Vib.* 452 (2019) 169–190.
- [26] Muxiao Li, Ziwei Zhu, Tiesong Deng, Xiaozhen Sheng, An investigation into high-speed train interior noise with operational transfer path analysis method, *Railw. Eng. Sci.* 29 (2021) 1–14.
- [27] Frederik Vanhollebeke, Joris Peeters, Dirk Vandepitte, Wim Desmet, Using transfer path analysis to assess the influence of bearings on structural vibrations of a wind turbine gearbox, *Wind Energy* 18 (5) (2015) 797–810.
- [28] Ahmed Hammami, Alfonso Fernandez del Rincon, Fakher Chaari, Fernando Viadero Rueda, Mohamed Haddar, Transfer path analysis of planetary gear with mechanical power recirculation, in: *Rotating Machinery and Signal Processing: Proceedings of the First Workshop on Signal Processing Applied To Rotating Machinery Diagnostics, SIGPROMD'2017*, April 09–11, 2017, Setif, Algeria 1, Springer, 2019, pp. 104–115.
- [29] He Dai, Xinhua Long, Feng Chen, Jie Bian, Experimental investigation of the ring-planet gear meshing forces identification, *J. Sound Vib.* 493 (2021) 115844.
- [30] Karl Janssens, Peter Gajdatsky, Ludo Gielen, Peter Mas, Laurent Britte, Wim Desmet, Herman Van der Auweraer, OPAX: A new transfer path analysis method based on parametric load models, *Mech. Syst. Signal Process.* 25 (4) (2011) 1321–1338.
- [31] Dennis de Clerk, Alexander Ossipov, Operational transfer path analysis: Theory, guidelines and tire noise application, *Mech. Syst. Signal Process.* 24 (7) (2010) 1950–1962.
- [32] Yanyan Nie, Fangyi Li, Liming Wang, Jianfeng Li, Mingshuai Sun, Mengyao Wang, Jianyong Li, A mathematical model of vibration signal for multistage wind turbine gearboxes with transmission path effect analysis, *Mech. Mach. Theory* 167 (2022) 104428.
- [33] Xiaoluo Yu, Zhanwei Li, Qingbo He, Yang Yang, Minggang Du, Zhike Peng, Gearbox fault diagnosis based on bearing dynamic force identification, *J. Sound Vib.* 511 (2021) 116360.
- [34] Yifan Huangfu, Xingjian Dong, Xiaoluo Yu, Kangkang Chen, Zhanwei Li, Zhike Peng, Fault tracing of gear systems: An in-situ measurement-based transfer path analysis method, *J. Sound Vib.* 553 (2023) 117610.
- [35] Maarten V. van der Seij, Dennis De Clerk, Daniel J. Rixen, General framework for transfer path analysis: History, theory and classification of techniques, *Mech. Syst. Signal Process.* 68 (2016) 217–244.
- [36] Xiaoluo Yu, Yifan Huangfu, Qingbo He, Yang Yang, Minggang Du, Zhike Peng, Gearbox fault diagnosis under nonstationary condition using nonlinear chirp components extracted from bearing force, *Mech. Syst. Signal Process.* 180 (2022) 109440.
- [37] Matthias Wegerhoff, Roland Sottek, Haiko Brücher, A Bridging Technology to Combine Test and Simulation with In-Situ TPA, Technical Report, SAE Technical Paper, 2020.
- [38] J.W.R. Meggitt, A.T. Moorhouse, In-situ sub-structure decoupling of resiliently coupled assemblies, *Mech. Syst. Signal Process.* 117 (2019) 723–737.
- [39] Laurent Keersmaekers, Luc Mertens, Rudi Penne, Patrick Guillaume, Gunther Steenackers, Decoupling of mechanical systems based on in-situ frequency response functions: The link-preserving, decoupling method, *Mech. Syst. Signal Process.* 58 (2015) 340–354.
- [40] Zengwei Wang, Ping Zhu, Zhao Liu, Relationships between the decoupled and coupled transfer functions: Theoretical studies and experimental validation, *Mech. Syst. Signal Process.* 98 (2018) 936–950.
- [41] Zengwei Wang, Zhike Peng, Chao Liu, Xi Shi, Virtual decoupling of mechanical systems considering the mass effect of resilient links: Theoretical and numerical studies, *Mech. Syst. Signal Process.* 123 (2019) 443–454.
- [42] Zengwei Wang, Long Cheng, Songtao Lei, Yi Yang, Lei Ding, An in-situ decoupling method for discrete mechanical systems with rigid and resilient coupling links, *Appl. Acoust.* 195 (2022) 108853.
- [43] Xuhui Liao, Shunming Li, Lianying Liao, Haodong Meng, Virtual decoupling method: a novel method to obtain the FRFs of subsystems, *Arch. Appl. Mech.* 87 (2017) 1453–1463.
- [44] Janko Slavić, Aleksandar Brković, Miha Boltežar, Typical bearing-fault rating using force measurements: application to real data, *J. Vib. Control* 17 (14) (2011) 2164–2174.
- [45] Per Christian Hansen, *Discrete Inverse Problems: Insight and Algorithms*, SIAM, 2010.
- [46] D. Calvetti, S. Morigi, L. Reichel, F. Sgallari, Tikhonov regularization and the L-curve for large discrete ill-posed problems, *J. Comput. Appl. Math.* 123 (1–2) (2000) 423–446.
- [47] Xiaoluo Yu, Changming Cheng, Yang Yang, Minggang Du, Qingbo He, Zhike Peng, Maximally weighted iteration for solving inverse problems in dynamics, *Int. J. Mech. Sci.* 247 (2023) 108169.
- [48] Hyoung Gil Choi, Anand N. Thite, David J. Thompson, Comparison of methods for parameter selection in Tikhonov regularization with application to inverse force determination, *J. Sound Vib.* 304 (3–5) (2007) 894–917.

- [49] Peng-Fei Li, Xi-Feng Tong, A pre-processing hybrid algorithm for solving ill-conditioned linear equations, in: 2011 International Conference on Machine Learning and Cybernetics, vol. 2, IEEE, 2011, pp. 810–813.
- [50] Omar D. Mohammed, Matti Rantatalo, Gear fault models and dynamics-based modelling for gear fault detection—A review, *Eng. Fail. Anal.* 117 (2020) 104798.
- [51] Xiaoluo Yu, Yang Yang, Qingbo He, Minggang Du, Zhike Peng, Multiple frequency modulation components detection and decomposition for rotary machine fault diagnosis, *IEEE Trans. Instrum. Meas.* 71 (2021) 1–10.
- [52] Xingkai Yang, Peng Zhou, Ming J Zuo, Zhigang Tian, Zhike Peng, The effect of time-varying operating condition on the crack induced impulses and its application to gearbox tooth crack diagnosis, *Mech. Syst. Signal Process.* 188 (2023) 110026.
- [53] Yang Yang, Z.K. Peng, X.J. Dong, W.M. Zhang, G. Meng, General parameterized time-frequency transform, *IEEE Trans. Signal Process.* 62 (11) (2014) 2751–2764.
- [54] Zhiguo Wan, Hongrui Cao, Yanyang Zi, Wangpeng He, Yimin Chen, Mesh stiffness calculation using an accumulated integral potential energy method and dynamic analysis of helical gears, *Mech. Mach. Theory* 92 (2015) 447–463.
- [55] Bing Yuan, Shan Chang, Geng Liu, Lehao Chang, Lan Liu, Quasi-static analysis based on generalized loaded static transmission error and dynamic investigation of wide-faced cylindrical geared rotor systems, *Mech. Mach. Theory* 134 (2019) 74–94.
- [56] Yifan Huangfu, Kangkang Chen, Hui Ma, Xu Li, Hongzheng Han, Zhifang Zhao, Meshing and dynamic characteristics analysis of spalled gear systems: A theoretical and experimental study, *Mech. Syst. Signal Process.* 139 (2020) 106640.
- [57] Shenghua Xie, Qungui Du, Yuhang Hu, Nonlinear dynamic modeling and analysis of spur gears considering dynamic contact state under misalignment errors, *Int. J. Non-Linear Mech.* 152 (2023) 104401.
- [58] Dooho Lee, Tae-Soo Ahn, Hyeon-Seok Kim, A metric on the similarity between two frequency response functions, *J. Sound Vib.* 436 (2018) 32–45.
- [59] Haoran Dong, Gang Yu, Qingtang Jiang, Time-frequency-multisqueezing transform, *IEEE Trans. Ind. Electron.* (2023).
- [60] You Jia, Zhichun Yang, Ning Guo, Le Wang, Random dynamic load identification based on error analysis and weighted total least squares method, *J. Sound Vib.* 358 (2015) 111–123.